UNIVERSITA’ DEGLI STUDI DI MILANO &
UNIVERSITA’ CATTOLICA DEL SACRO CUORE

Dipartimento di Matematica e Fisica

Corso di Dottorato di Ricerca in Fisica, Astrofisica e Fisica Applicata
Ciclo XXVII

Unfolding the ultrafast interplay between delocalized wavefunctions and localized electronic interactions in quantum correlated materials

Settore Scientifico Disciplinare FIS/03

Tesi di Dottorato di:
Simone Peli

Supervisore:
Dott. Claudio GIANNETTI
Coordinatore:
Professor Marco BERSANELLI

Anno Accademico 2013/2014

Copyright © 2015 Simone Peli

UNFOLDING THE ULTRAFAST INTERPLAY BETWEEN DELOCALIZED WAVEFUNCTIONS AND LOCALIZED ELECTRONIC INTERACTIONS IN QUANTUM CORRELATED MATERIALS

PhD. Thesis - Physics, Astrophysics and Applied Physics PhD School - Milano

Printing, January 2015, Milano, Italy

Contents

1 Strongly Correlated Materials 15
1.1 Energy scale W,U and SO 15
1.2 Mott-Hubbard Insulators 21
1.3 Charge Transfer Insulators 21
1.4 t-J Model 22

2 Cuprates 25
2.1 Electronic Structure CuO 26
2.2 Cuprate Phase Diagram 28
2.3 Pseudogap Phase 31
2.4 Non-Fermi liquid Phase and Quantum Criticality 34

3 Optical Spectroscopy at equilibrium 37
3.1 Drude Lorentz Model 37
3.2 Extended Drude Model 38
3.3 Spectral Weight 40
3.4 Temperature and Doping Dependence of Cuprates Optical Properties 42

4 ARPES 47
4.1 Three step model 49
4.2 Fermi Surface 51
4.3 Metal-Insulator Transition 53

4.4 Laser ARPES 54
4.5 Laser ARPES setup 54
4.6 Laser ARPES measurements on Bi2212 56

5 Experimental Systems 61
5.1 Optical Oscillator 61
5.2 Optical Parametric Amplifier 63
5.3 XUV-Laser Photoemission 69

6 Ultrafast spectroscopy on the doped single-layer copper oxide Bi2201 73
6.1 Electronic structure 73
6.2 Doping 73
6.3 Optical Properties at Equilibrium 77
6.4 Optical Properties Out Of Equilibrium 87
6.5 Time- and Frequency-resolved Data 91
6.6 Data Analysis 95

7 UV time-resolved photoemission on the doped double-layer copper oxide Bi2212 115
7.1 Electronic structure 116
7.2 Optical properties at equilibrium 117
7.3 Doping and Temperature Dependence of the O-2p_π band. 119
7.4 Time-Resolved ARPES Measurements 123
7.5 Data Analysis 124
7.6 Discussion and Conclusions 127

8 Conclusions 135

Bibliography 137

List of Publications 155

Acknowledgements 157

Dedicated to little Camilla.

Introduction

Quantum materials are solid state systems that, when subjected to extreme temperatures and pressures, exhibit interesting features like superconductivity, but also unusual forms of magnetism, exotic phase transitions, and other physical qualities we are only beginning to understand. In many of these materials the electron-electron interactions play a central role in determining their electronic, magnetic, optical, and sometimes even mechanical properties. These systems are often referred to as *quantum correlated materials*.

In conventional materials, such as common metals and semiconductors, the energy of the short-range (i.e. between two electrons occupying the same lattice site) electron-electron interactions is negligible as compared to the kinetic energy of the electrons. In this case, the electrical, mechanical, and thermal properties may all be understood reasonably well adopting the independent-electron approximation, in which the interactions among the electrons are treated as an average perturbation of the single-electron properties. On the contrary, in many of the transition metals with partially filled $3d$ orbitals, the strong Coulomb repulsion forces the electrons to reside on spatially separated orbitals, abruptly decreasing their kinetic energy and their mobility. In general, the interplay between electron-electron interactions, lattice structure, kinetic energy, and magnetic degrees of freedom is incredibly complex. The result is a competition between distinct ground states, with different symmetries and low energy excitations. Furthermore the properties of this materials strongly depend on the interplay between the ”local” (in real space) correlations and the delocalized wavefunctions describing the Bloch orbitals and other many-body collective excitations. New phases often appear near ”quantum phase transitions”, when tuning a parameter such as electronic population (doping) or magnetic field tips the balance between one energy scale and one of its competitors. These phases can have surprising and useful properties, such as high temperature superconductivity. The potentiality of such materials stays in the fact that a little modification of the external controllable parameters (doping, pressure, temperature) can have dramatic consequences on their properties. For these reasons, and for the their potentially immense technological relevance, the attention of the scientists Has been attracted by these materials since their discovery.

In the present thesis we focus on a family of materials that, probably, is the most studied in the last thirty years: *cuprates*. They are layered copper oxide compounds that can sustain superconductivity at unexpectedly high temperatures. This important property has been discovered by Bednorz and Muller in 1986 [Bednorz and Müller, 1986] and soon after, the critical temperature T_C of these doped copper oxide-based compounds exceeded the boiling temperature of the liquid nitrogen, rapidly rising significantly above 100 K. For this reason these materials are often known as high temperature superconductors (HTCs). From the theoretical point of view, while the conventional superconductors are well described within the framework of the BCS theory (Bardeen, Cooper and Schrieffer [Bardeen et al., 1957]), the comprehension of the nature and the origin of the microscopic mechanism leading to the high-temperature superconductivity in HTCs is still lacking.

Beside the superconductivity, the phase diagram of the cuprates presents wealth of very interesting phases. When undoped, cuprates are charge-transfer insulators, in contrast to the predictions of the conventional band-theory within the independent-electron approximation, with an antiferromagnetic order. When doped, the system enters the so-called pseudogap region, defined by a $T^*(p)$ line and exhibits the spontaneous tendency to charge and spin ordering. The pseudogap is characterized by the presence of a d-wave gap, even though superconductivity is absent. The debate whether this state is a precursor or compete with the superconductivity is still open. Embedded in the pseudogap there is a mosaic of exotic electronic phases with various symmetry-broken ground states characterized by charge ordering: the tendency of the valence electrons to segregate in periodically-modulated structures. Recently, different equilibrium techniques (Resonant X-ray scattering, Angle Resolved Photoemission, Scanning Tunnelling Microscopy...) have shown that all these orders, together with the pseudogap line, vanish at T=0 at a precise doping level around the optimal doping. This point of the phase diagram is called *quantum critical point* (QCP). In the overdoped regime, from the QCP a strange metal phase originates, characterized by the absence of quasiparticles and a linear dependence of the resistivity with the temperature, in contrast to the T^2 dependence predicted by the Landau Fermi-liquid for conventional metals. Despite this results, the QCP remains mysterious and inaccessible by equilibrium techniques, because of the low temperature and the extremely high instability of the several orders that takes origin from it.

Here, we tackle the problem of the origin of the quantum critical point from a non-equilibrium perspective, by using the ultrafast optical pump-probe technique. The scope is to disentangle the electronic dynamics from the thermal dynamics, since the first happens on timescales much shorter than thermal heating, being the latter related to the thermalization with the phonons. The first pioneering pump-probe experiments performed a single probe photon energy (1.55 eV, i.e., 800 nm, the fundamental of conventional Ti:Sapphire lasers). However, the knowledge of the dynamics at only one wavelength was not sufficient to unveil the microscopic mechanisms at the origin of the time-resolved optical signal. Therefore, in this work we will adopt broadband time-resolved techniques which allow the simultaneous access to a broad part of the optical dielectric function. The main experimental data have been obtained by an Optical Parametric Amplification-based system by which we probe the dynamics of the optical properties in the visible region 1.8-2.4 eV and with a temporal resolution of $\sim$ 6 fs. Also, we have used a microstructure optical fiber seeded by the output of a Ti:Sapphire laser to generate supercontinuum spectrum in the energy range 1.1-2.3 eV with a temporal resolution of $\sim$ 100 fs. Thanks to these novel techniques we could investigate the behaviour of high-energy optical properties (>2 eV) of a single-layer copper oxide Bi2201. By studying the dynamics of the charge-transfer process as a function of the doping, we unveiled an unexpected and fundamental property of cuprates. Even at room temperature, these systems undergo a transition from an insulating-like behaviour, in which the charge-transfer process is localized in real space, to a more conventional behaviour in which the final state of the high-energy optical transitions is delocalized over the lattice. Surprisingly, the doping at which we observe this transition at room temperature corresponds to the critical doping, p_{cr}, at which the pseudogap $T^*(p)$ line dies at $T = 0$ (the quantum critical point). These results demonstrate that the quantum critical point, from which the different ordering tendencies emerge, is determined by a more general property of the ground state which is already present at higher temperatures and can be unveiled when the system is driven out of equilibrium.

The second goal of the present work was to investigated the role of the high-energy excitation process (>1.5 eV) in transiently modifying the occupation of both the conduction band and the deeper bands related to the oxygen orbitals in double layer copper oxide Bi2212. To this aim, we combined the pump probe technique to the XUV photoemission technique which probes the transient occupation of the states. Preliminary measurements have been performed in the ARPES Laboratory of UBC (Vancouver) using a traditional laser-

ARPES system where the probe is obtained via harmonic generations of a Ti:Sapphire oscillator output reaching 6 eV photon energy. After that, we have performed the core of the experiments at the XUV time-resolved photoemission beamline ARTEMIS at the Central Laser Facilities in UK. With this technique it is possible to generate high harmonics using a laser pulse in a gas jet and use such harmonics (10-100 eV) to do a photoemission experiment. We have measured, for the first time, the ultrafast dynamics of the oxygen bands, unveiling an unexpected bottleneck in the relaxation of the holes photoexcited in the O-$2p_\pi$ band at (π, π) point of the Brillouin zone at 1.5 eV binding energy. This phenomenon can be understood by considering the antibonding nature of the O-$2p_\pi$ bands which do not have any overlap with the $\mathrm{Cu}3d_{x^2-y^2}$ states of the conduction band.

These results can open a new way in the understanding of the exotic properties of quantum materials and provide a new point of view in looking at their temperature-doping phase diagram, investigating the dynamics of the high-energy excitations directly in the normal state which carries the seeds of unconventional superconductivity.

Outline

In this thesis we investigate the non-equilibrium optical response of two prototypical high-temperature superconductors, more precisely, of a $Bi_2Sr_{2-x}La_xCuO_{6+\delta}$ single-layer copper oxide (Bi2201) and $Bi_2Sr_2Ca_{0.92}Y_{0.08}Cu_2O_{8+\delta}$ double-layer copper oxide (Bi2212). The optical spectroscopy technique used in this work, is characterized by both spectral and temporal resolution and exploits the large spectral content of the supercontinuum light produced by a non-linear photonic crystal fiber and an OPA-based system. Besides these optical techniques we have also performed photoemission experiments using a XUV pulsed probe obtained exploiting the harmonic generation in a gas jet. More precisely, we used these non-equilibrium techniques to explore the following aspects:

- Which physical parameters determines the critical doping at which the low-temperature QCP emerge? Is it possible to observe a signature of the QCP at high-temperatures by driving the system strongly out of equilibrium? Is there any relation between the dynamics of the optical properties and the QCP? Is the high-energy scale corresponding to the charge-transfer excitations involved?

- How is the band occupation perturbed after the excitation with a near-IR ultrafast pulse? Is there any selective modification in the *k*-space of the conduction band and of the oxygen bands at 1.5 eV binding energy? Which is the relation between the dynamics of the holes injected in the oxygen band and of the electrons promoted to the conduction band?

The work has been organized in the following way:

Chapter 1 A general overview on the energies involved in the tight-binding, Mott-Hubbard and J-eff models is given. These energies are the yardstick to discern between weakly and strongly correlated materials. A more detailed description of the single- and multi-band Hubbard model is given.

Chapter 2 In this chapter we present the general crystal and electronic structure of the cuprates. Furthermore we describe in detail the cuprate phase diagram and we provide a description of the different orders and phases (pseudogap, strange metal, charge ordering, quantum critical point) emerging at low temperature and doping.

Chapter 3 We report and discuss the models used to describe the optical properties of these materials, in particular we will focus on the Drude-Lorentz and the Extended Drude model. We also discuss the doping and temperature evolution of the optical properties of cuprates.

Chapter 4 An introduction to the conventional and time-resolved Angular Resolved Photoemission Spectroscopy (ARPES) is given.We provide description of the tr-ARPES setup at the ARPES Laboratory of the University of British Columbia in Vancouver. I have developed the optical setup to couple with the pre-existent ARPES chamber during the second year of my PhD.

Chapter 5 We give a detailed overview on the different techniques used, in particular: optical oscillator Ti:Sapphire-based system, Optical Parametric Amplifier system and XUV tr-ARPES. These experimental setups are located in Universita' Cattolica del Scaro Cuore (Brescia), Politecnico (Milano) and Central Laser Facilities (UK) respectively.

Chapter 6 We report the data obtained on the single-layer copper oxide $Bi_2Sr_{2-x}La_xCuO_{6+\delta}$ through time-resolved optical spectroscopy experiments. As a first step we introduce Bi2201 crystal and electronic structure and we describe the doping process. We present the equilibrium optical properties of this material and we provide a detailed analysis of the experimental transient reflectivity experiments. At the end of the chapter an interpretation and a discussion of the results is also given.

Chapter 7 We present the experimental data of XUV time- and angular-resolved photoemission spectroscopy on the double-layer copper oxide $Bi_2Sr_2Ca_{0.92}Y_{0.08}Cu_2O_{8+\delta}$. The equilibrium optical properties of the material are described together with their evolution in doping and temperature. We present the data and a detailed analysis of them. Finally we provide our proposed interpretation of the results.

Chapter 8 Conclusions

1 Strongly Correlated Materials

1.1 Energy scale W,U and SO

In the *tight-binding* approximation [Kittel, 1986], the interaction between nearby atomic orbitals leads to the formation of energy bands. These energy bands are originated by the coulomb interaction between the atom cores and the electron. Each state of given quantum number of the free atom is spread in the crystal into a band of energies.

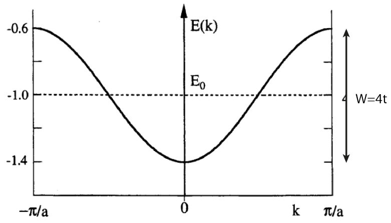

Figure 1.1: Energy band $E(k) = E_0 + 2t\cos(ka)$ for a tight-binding model with a single orbital per site and nearest neighbour interactions [Grosso and Parravicini, 2000].

Let us consider a one-dimensional crystal made by equal atoms centered in the lattice position i. Each of this atoms contributes with just one local orbital ϕ_a with a ground state energy E_a. If we consider the hopping just between nearest neighbour sites we have that the diagonal matrix elements of H are all equal and the same happens with the hopping integrals between nearest neighbour orbitals. We have:

$$\langle \phi_a(x-x_i)|H|\phi_a(x-x_i)\rangle = E_0 \qquad \langle \phi_a(x-x_i)|H|\phi_a(x-x_{i\pm 1})\rangle = t \tag{1.1}$$

If the influence of one atom to another is small, we obtain an approximate wavefunction for one electron in the whole crystal by:

$$\Psi_\sigma(k,x) = \frac{1}{\sqrt{N}}\sum_i e^{ikx_i}\phi_a(x-x_i)\chi(\sigma) \tag{1.2}$$

The state which describes those electrons are characterized by two good quantum numbers: the number vector $\mathbf{k}$ and the spin σ. The expression for the Hamiltonian reads:

$$H = -\frac{\hbar^2}{2m}\frac{\mathrm{d}^2}{\mathrm{d}x^2} + V(x) \tag{1.3}$$

where $V(x)$ is the crystal potential sketched in Figure 1.2 b).
Avoiding the spin part, the energy dispersion of the energy band originated from atomic orbitals ($\phi_a(x-x_i)$) due to the presence of the crystal potential is thus given by:

$$E(k) = \langle \Psi(k,x)|H|\Psi(k,x) = \frac{1}{N}\sum_i\sum_j e^{ik(x_i-x_j)}\langle \phi_a(x-x_i)|H|\phi_a(x-x_j)\rangle \tag{1.4}$$

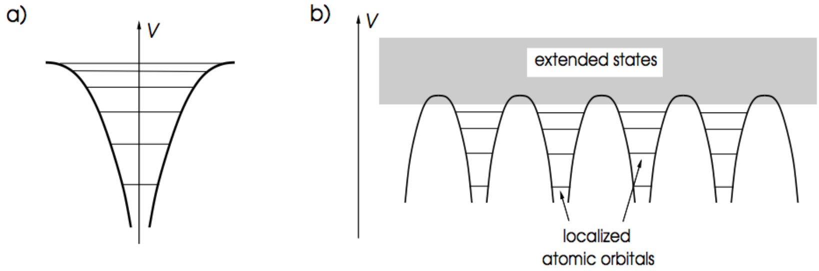

Figure 1.2: a) Single atomic Coulomb potential yields to discrete spectrum of electronic states. b) Atoms arranged in a regular lattice give rise to a periodic potential. Electron states of low energy can be considered as localized at the atom sites. The higher energy states, however, extend further and can delocalize to form itinerant electron states which form bands.

Now, distinguishing between the two cases $i = j$ and $i \neq j$ and using the relations 1.1 one obtains the following dispersion expression:

$$E(k) = E_0 + 2t\cos(ka) \tag{1.5}$$

This shows at the most elementary level that the N degenerate states of non-interacting atoms are smeared into a continuous band of width $W = 4|t|$ (Figure 1.1), where t is the so called *hopping integral* and reads:

$$t_{ij} = \int \mathrm{d}x \phi_a^*(x - x_i)\left[-\frac{\hbar^2}{2m}\frac{\mathrm{d}^2}{\mathrm{d}x^2} + V(x)\right]\phi_a(x - x_j) \tag{1.6}$$

Just to give an example of the energy scale of the hopping integral t in metals, at a constrained separation of 7 Å , the bandwidth of the sodium s-band amounts to approximately 1.4 eV [Seitz, 1940] yielding a value for the hopping integral of nearly 0.35 eV.

In the previous picture we can distinguish the case that there is an *odd* or an *even* number of electrons per atom (unit cell):

Even The bands can be either empty or completely filled. There is a finite energy needed (E_g) to add to excite one electron and the material is called *insulator*.

Odd The last band is not completely filled then the system is a *metal*. There is not energy gap to overcome to excite the electrons. Electrons can move and excitations with arbitrarily small energies are possible. (Figure 1.3)

So far we have seen that the quantum mechanical description of electrons in solids - the band theory, developed in the late 1920_s ([Bethe, 1928] [F.Bloch, 1929]) - offered a straightforward account for distinctions between insulators and metals. In this approach, electrons are considered to move independently in a periodic background potential (Hartree-Fock approximation) but we know that electron-electron interaction is crucial in understanding the important properties of some materials [F.Mott, 1990] [Mott and Peierls, 1937].

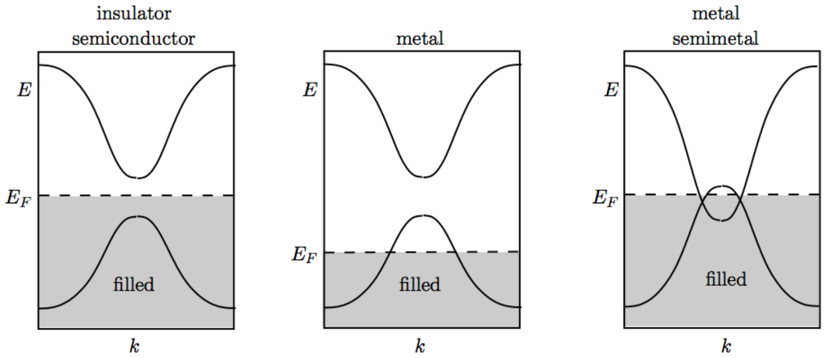

Figure 1.3: Material classes according to band filling: left panel: insulator or semiconductor (partially filled bands with the Fermi level in band gap); center panel: metal (Fermi level inside band); right panel: metal or semimetal (Fermi level inside two overlapping bands).

In particular, high-temperature superconductivity turns out to be impossible to explain within the Hartree-Fock approximation. As an example we cite CoO. If we treated it within the independent electron approximation we would find that this substance is metallic, with an odd number of electrons per unit cell and a partially filled d band [1]. In reality CoO is an insulator because the strong electron correlations suppress the charge fluctuations required to have a non-vanishing conductivity. So, in order to take into account the electron correlations in those materials, we need to introduce a new energy scale U. The Hubbard model [Hubbard, 1964] is believed to capture the main part of the physics of the strongly correlated materials. To give a better way to compare the tight-binding model with the Hubbard model it is useful to rewrite the tight-binding wave function of one electron bounded to site i in a second quantization 3D picture:

$$\phi_a(\mathbf{r}-\mathbf{R}_i)\chi(\sigma) = c^\dagger_{i\sigma}|0\rangle \tag{1.7}$$

where we have changed the coordinates from 1D to 3D and we added the spinor function $\chi(\sigma)$. $c^\dagger_{i\sigma}$ is the *creation operator* that creates one electron with spin σ on the site i. At this point the tight-binding hamiltonian can be rewrite in the following way:

$$H_t = -\sum_{ij\sigma} t_{ij} c^\dagger_{i\sigma} c_{j\sigma}, \qquad t_{ii} = 0, \qquad t_{ij} = t_{ji} \tag{1.8}$$

The hopping hamiltonian is the sum over all hopping processes: $c_{j\sigma}$ destroys an electron on lattice site j and $c^\dagger_{i\sigma}$ creates the electron on site i. As a good approximation we can reduce the sum only between nearest neighbour sites so that $j = i \pm 1$. Now we can introduce the electron-electron correlations. The most important interaction is between two electrons on the same site that have experience of a strong Coulomb repulsions between each other. because of the Pauli exclusion principle there can maximally be only two electrons

[1] Co atom has electron configuration $3d4s$, and the O atom $2s2p$, so the number of electrons per unit cell is $9+6=15$, an odd number.

per atom with opposite spins. The correlation energy between two electrons on the same site is given by:

$$U = \int d\mathbf{r}_1 d\mathbf{r}_2 |\phi_a(\mathbf{r}_1)|^2 \frac{e^2}{|\mathbf{r}_1 - \mathbf{r}_2|} |\phi_a(\mathbf{r}_2)|^2 \tag{1.9}$$

and this energy can emerges only when a single site is doubly occupied. So we can define the interaction hamiltonian as the sum over all the doubly occupied sites:

$$H_U = U \sum_i n_{i\uparrow} n_{i\downarrow} \tag{1.10}$$

where $n_{i\sigma} = c^\dagger_{i\sigma} c_{i\sigma}$ is the electron number operator for spin σ on the site i. $n_{i\sigma}$ can assume just the values 0 or 1. So, the product $n_{i\uparrow} n_{i\downarrow}$ is non vanishing only when, on the site i there are one electron with spin up together with one with spin down. Finally, the *one band Hubbard hamiltonian* is the sum of the two terms:

$$H = H_t + H_U = -\sum_{ij\sigma} t_{ij} c^\dagger_{i\sigma} c_{j\sigma} + U \sum_i n_{i\uparrow} n_{i\downarrow} \tag{1.11}$$

Note that differently by the tight binding states, the wave number $\mathbf{k}$ is no longer a good quantum number substituted by the position i of the particle on the lattice sites. On the other side, the spin is still a good quantum number. Starting from this hamiltonian we can identify two limiting behaviours: 1) when $t \gg U$ we go back to the electrons independent approximation and to the tight-binding model; 2) when $t \ll U$ the electrons are strongly correlated and they lose their itinerant character. In the weak correlation limit a metallic state is observed, while in the strong correlation limit the one-band model splits into two Hubbard subbands that reflects the cost in energy for adding a second electron on an already occupied site (Figure 1.4).

The transition between the two limits refers to the *metal-insulator transition* [Imada et al., 1998] For the half-filled case (characterizing by an average occupation electron number $n = 1$) the model describes a *Mott-Hubbard insulating* state [Mott, 1949][F.Mott, 1956]. The Hubbard model well describes those elements carachterized by localized outer orbitals as $3d$ and $4f$ because their energy bands are narrow (~ 3 eV) in comparison with the strong Coulomb repulsion between electrons which is of the order of $\sim 8 - 10$ eV [Antonides et al., 1977]. Now, if we move in the periodic table of elements towards heavier elements a new energy scale get more important: the *spin-orbit coupling*. Electrons, moving on an orbital, have a total orbital momentum L that can be coupled to their spin S momentum giving a *total angular momentum* $J = S + L$. So, spin-orbit coupling is a relativistic effect, which provides an interaction between the orbital angular

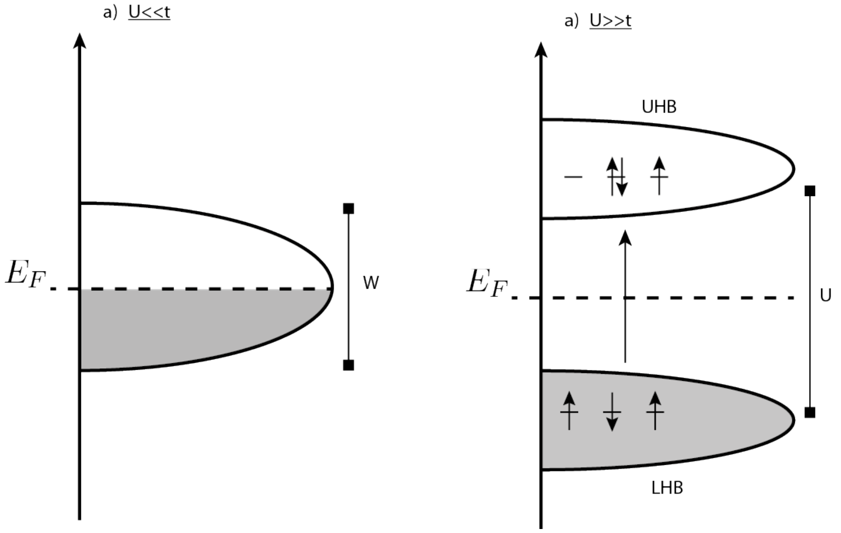

Figure 1.4: In the half-filling case, when the electronic correlations are weak (a) the system is a metal with half-filled band. When the correlations are strong (b) an energy gap U is present due to the energy cost in creating a doubled occupation.

momentum and electron spin in atoms, and is usually considered a small perturbation in the discussion of electrons in solid. However, in heavy elements it need not be weak (it effectively increases proportionally to Z^4 [Witczak-Krempa et al., 2014], where Z is the atomic number) and indeed has striking qualitative effects. In the heavy transition metal compounds characterized especially by $5d$ and $4d$ orbitals, the influence of both the electronic on-site interaction U and the spin-orbit coupling has to be taken into account. Descending the periodic table of elements from $3d$ to $4d$ to $5d$ series, there are several competing trends. First, the d orbitals become more extended tending to reduce the electronic repulsion U and thus quenching the correlation effects. Simultaneously, the spin-orbit coupling increases dramatically, leading to enhanced splitting between otherwise degenerate orbitals and bands, reducing in may case the kinetic energy. Including the spin-orbit coupling in this picture, the hamiltonian that describes these electrons becomes:

$$H = -\sum_{ij\sigma} t_{ij} c^{\dagger}_{i\sigma} c_{j\sigma} + U \sum_{i} n_{i\uparrow} n_{i\downarrow} + \lambda \sum_{i} \mathbf{L}_i \cdot \mathbf{S}_i \tag{1.12}$$

where λ is the spin-orbit coupling between spin $\mathbf{S}$ and angular momentum $\mathbf{L}$. As an example of these competing energy scale in real materials we can bring the Sr_2IrO_4 [Kim et al., 2008]. Considering its odd number of electrons per unit formula ($5d^5$), one expect a metallic state in a band picture. Unexpectedly it is an insulator [Crawford et al., 1994]. It is natural to consider the spin-orbit coupling responsible of this insulating nature since its energy is much larger than in $3d$ and $4d$ orbitals. This coupling can largely modify the states near Fermi energy E_F in $5d$ orbitals but also correlation effect can be important when associated to a large spin-orbit coupling to give origin to a new Mott instability. Under the crystal symmetry the $5d$ states are split into t_{2g} and e_g orbital states by the crystal field energy (Figure 1.5) and the system would become a metal with partially filled t_{2g} band. In the strong spin-orbit coupling the t_{2g} band splits into effective total angular momentum $J_{eff} = 1/2$ doublet and $J_{eff} = 3/2$ quartet. As a result, with the filled $J_{eff} = 3/2$ band and one remaining electron in the $J_{eff} = 1/2$ band, the system is effectively reduced to a half-filled $J_{eff} = 1/2$ single band. At this point, even a small U can open a gap, making it a $J_{eff} = 1/2$ Mott insulator. In Sr_2IrO_4 the spin-orbit coupling is ~ 0.4 eV [Kim et al., 2008]. The emergent behavior of the $J_{eff} = 1/2$ Mott insulator has been explored in experiments such as angle resolved photoemission spectroscopy [Kim et al., 2008] [Comin et al., 2012], optical conductivity [Moon et al., 2009], resonant x-ray scattering [Kim et al., 2009], and resonant inelastic x-ray scattering [Ishii et al., 2011]. In this scenario the spin is not a good quantum number any more but we have to introduce the effective total angular momentum J_{eff} which will characterize the eigenstates of the spin-orbit hamiltonian [Onishi, 2012].

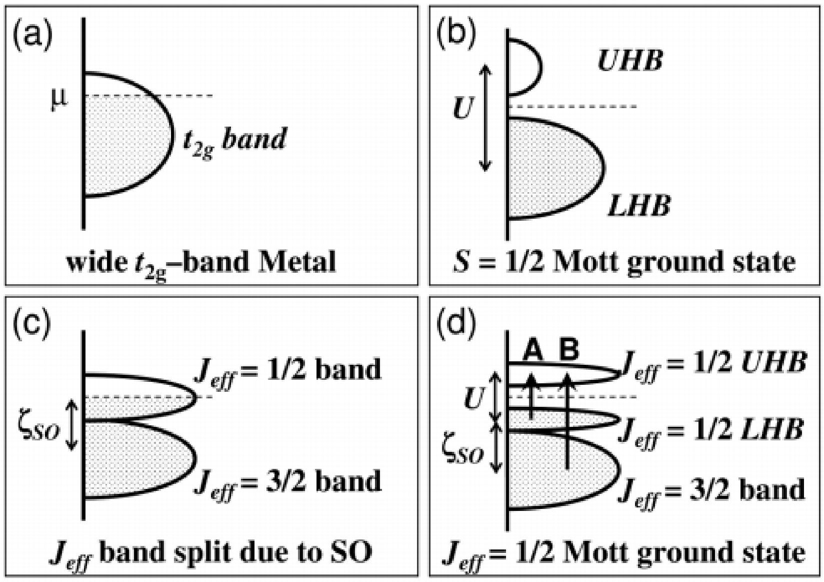
(a)
μ
t_{2g} band
wide t_{2g}–band Metal
(b)
UHB
U
LHB
S = 1/2 Mott ground state
(c)
J_{eff} = 1/2 band
ζ_{SO}
J_{eff} = 3/2 band
J_{eff} band split due to SO
(d)
A B
J_{eff} = 1/2 UHB
U
J_{eff} = 1/2 LHB
ζ_{SO}
J_{eff} = 3/2 band
J_{eff} = 1/2 Mott ground state

Figure 1.5: Schematic energy diagrams for the $5d^5$ (t_{2g}) configuration (a) without spin-orbit and U, b) with large but non realistic U and no SO, c) with SO but not U, d) with SO and realistic U.

In conclusion, we have seen that the interplay between these three energy scales W,U and SO and the strength of one on the others needs a variety of different models to well describe the several experimental evidences. The following table can help to summarize the concepts:

Relative Energies	Elements	Theory	Absolute Energies
$SO, U \ll W$	Delocalized orbitals s and p	Band Theory	$W \sim 0.35$ eV
$SO, W \ll U$	Localized $3d$ orbitals	Hubbard Model	$U \sim 8 - 10$ eV
$SO \simeq W \simeq U$	$4d$ and $5d$ orbitals	J_{eff} model	$SO \sim 0.4$ eV

1.2 Mott-Hubbard Insulators

In the simplest approximation, one can consider a one-band model and take into account only the single-electron hopping matrix element t between the nearest neighbours and the largest single-site Coulomb energy U (Figure 1.6). In this approximation, the complicated resulting polar model Hamiltonian is reduced to the so-called Hubbard model [Hubbard, 1963]:

$$H = -t \sum_{i \neq j \sigma} c^{\dagger}_{i\sigma} c_{j\sigma} + U \sum_{i} n_{i\uparrow} n_{i\downarrow} \tag{1.13}$$

where $c^{\dagger}_{i\sigma}(c_{i\sigma})$ are the creation (annihilation) operators for electrons of spin $\sigma = (\uparrow, \downarrow)$ at the lattice site i and $n_{i\sigma} = c^{\dagger}_{i\sigma} c_{i\sigma}$ is the electron occupation number. This model allows the consideration of the cases of both weak correlations, $U \ll W$, and strong correlations, $U \gg W$, where $W = 2zt$ is the bandwidth (z is the number of nearest neighbors, $z = 4$ for a square lattice). In the weak correlation limit a metallic state is observed, while in the strong correlation limit the one-band model splits into two Hubbard subbands (see Figure 1.4). For the half-filled case (characterizing by an average occupation electron number $n = 1$) the model describes a Mott-Hubbard insulating state, which becomes an unconventional metal under the hole doping ($n < 1$) of the lower Hubbard subband (LHB), or under the electron doping ($n > 1$) of the upper Hubbard subband (UHB).

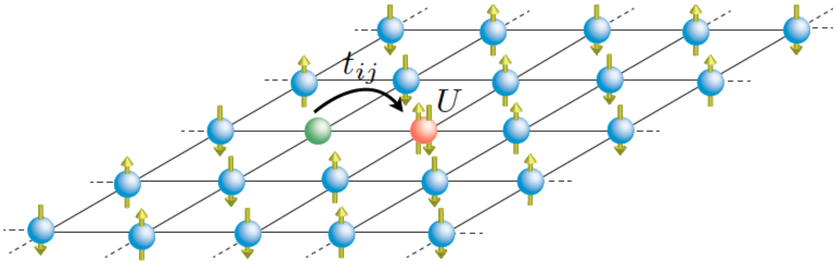

Figure 1.6: Background of the single band Hubbar model at half filling. The green site refers to an empty site while the red one is a double occupied site. The t_{ij} matrix element is the probability for one electron to hop on a neighbour site. U is the strong Coulomb repulsion that needs to be overcome to have a double occupation.

1.3 Charge Transfer Insulators

In the theoretical investigation of the many-body effects in copper-oxide superconductors, it is most frequently used a model more complicated than 1.13, namely, the three-band p-d effective Hamiltonian proposed by [Emery, 1987] and [Abrahams et al., 1987]. In the p-d model, to take into account the charge-transfer character of the insulating state, the copper and oxygen states in the CuO_2 plane are considered explicitly:

$$H = \sum_{i\sigma} \epsilon_i n_{i\sigma} + \sum_{i\neq j\sigma} t_{ij} c^{\dagger}_{i\sigma} c_{j\sigma} + \frac{1}{2} \sum_{i\sigma} U_i n_{i\sigma} n_{i-\sigma} + \frac{1}{2} \sum_{i\neq j\sigma\sigma'} U_{ij} n_{i\sigma} n_{j\sigma'} \quad (1.14)$$

Here, $c^{\dagger}_{i\sigma}$ are the creation (annihilation) operators for holes of spin σ at the copper or oxygen sites i of the square CuO_2 lattice, $n_{i\sigma} = c^{\dagger}_{i\sigma} c_{i\sigma}$, $\epsilon_i = (\epsilon_p, \epsilon_d)$ are the energies of the O-2$p_\sigma(x, y)$ states and Cu-3$d(x^2 - y^2)$ states, respectively, $t_{ij} = (\pm t_{pd}, \pm t_{pp})$ are the transfer integrals for p-d and p-p states on nearest Cu-O and O-O sites, respectively; $U_i = (U_d, U_p)$ are the on-site Coulomb repulsion energies for 3d and 2p states, and $U_{ij} = (U_{pd}, U_{pp})$ are the intersite Coulomb interactions. The Hamiltonian is written in the hole representation for the vacuum state defined by filled Cu-3d^{10} and O-2p^6 states. Figure 1.7 shows Cu-$d_{x^2-y^2}$ and bonding O-p_x, O-p_y in-plane orbitals in the CuO_4 cluster. The energy levels are sketched in the right panel: the local one-hole ϵ_d state and the two-hole $\epsilon_d + \epsilon_p$ and $2\epsilon_d + U_d$ states. The singlet two p-hole state with higher energy $2\epsilon_p$ is not shown. The ligand t_{pd} hybridization results in a repulsion of both the one-hole energy levels and the two-hole singlet energy levels as shown in the right part for $t_{pp} = 0$. Since the Coulomb repulsion U_d shifts up the energy of the d-hole singlet, the t_{pd} hybridization between three singlet states, p-p, d-d and p-d, leads to decrease of the lowest p-d singlet state energy. Because the energy of the p-d triplet state does not change, the singlet and triplet two-hole p-d states are split out. Therefore, the lowest two-hole state becomes the p-d singlet state ϵ_2: the Zhang-Rice singlet (ZR) [Zhang and Rice, 1988]. The excitation energy for transition from the one-hole d-like state ϵ_1 to the two-hole ZR singlet state ϵ_2 determines the charge transfer gap $\Delta_{pd} \simeq \epsilon_p - \epsilon_d$. The p-hole hybridization t_{pp} splits p-levels and the charge-transfer gap reduces to $E_{gap} = \Delta_{pd} - t_{pp}$ (see e.g. [Eskes et al., 1990]).

1.4 t-J Model

In the limit of a strong Coulomb repulsion, $U \gg t$, when the one-band in the Hubbard model splits into two subbands with a correlation gap $\Delta = U - W$ one can consider explicitly only the subband, which crosses the Fermi level. The other subband can be taken into account by a perturbation theory over $t/U \ll 1$. This results in a further reduction in the two-subband model to a one-subband t-J model. The important role of a strong Coulomb repulsion in super-

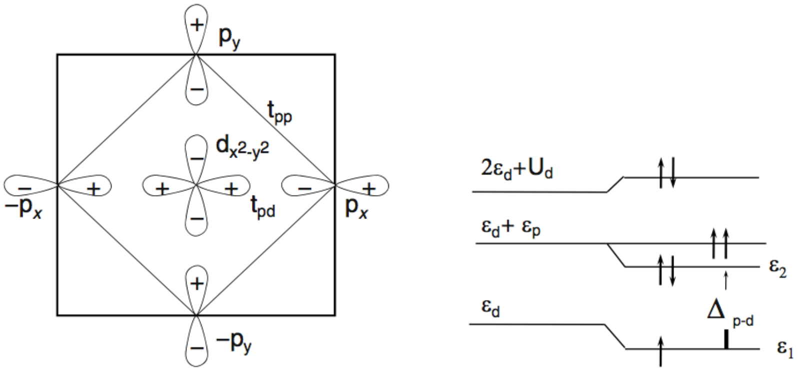

Figure 1.7: Cu-$d_{x^2-y^2}$ and bonding O-p_x, O-p_y in-plane orbitals in the CuO_4 cluster and copper ϵ_d and oxygen ϵ_p hole energy levels.

conducting cuprates was first pointed out by Anderson [Anderson, 1987] who proposed to study superconductivity in La_2CuO_4 compounds within the t-J model. The model has been derived earlier by a number of researchers (for review see e.g., [Ogata and Fukuyama, 2008]). The conventional form of the t-J model is:

$$H_{t-J} = \sum_{i \neq j, \sigma} t_{ij} c^{\dagger}_{i\sigma} c_{j\sigma} + \frac{1}{2} \sum_{i \neq j} J_{ij} \left(\mathbf{S}_i \mathbf{S}_j - \frac{1}{4} n_i n_j \right) \qquad (1.15)$$

where the exchange interaction can assume two forms: for the Hubbard model (1.13) $J_{ij} = 4t^2/U$, and for the effective *p-d* model (1.14) $J_{ij} = 4(t_{ij})^2/\Delta_{pd}$. The second part of the hamiltonian is identical to the antiferromagnetic Heisenberg model. The antiferromagnetism comes out from the possibility of the particles to virtually hop on a neighbour site. This hopping is forbidden when two near spins are parallel (because of the Pauli principle). if they are antiparallel, the system reduces its overall energy (see Figure 1.8). For this reason, the antiferromagnetism in the ground state of the half filled Hubbard model is energetically favourable.

In conclusion, we can argue that the model Hamiltonians for the CuO_2 plane considered above, in particular the three-band *p-d* model (1.14) contains enough physics to explain the many body-effects in cuprate superconductors caused by strong electron correlations.

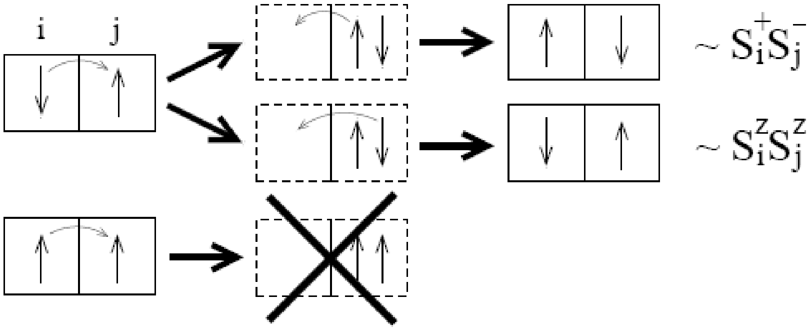

Figure 1.8: Hopping processes with a virtual doubly occupied site corresponding to the $S_i^z S_j^z$ and $S_i^+ S_j^-$ term of the Heisenberg hamiltonian. In the case of parallel spins virtual hopping is not possible.

2 Cuprates

The beginning of 1986 marked the inauguration of the cuprate superconductor epoch in the search for high-temperature superconductivity. The discovery by Karl Alex Müller and Johan Georg Bednorz of the occurrence of superconductivity in the lanthanum and barium copper oxides at temperatures up to 35K caused an unprecedented wave of scientific activity in the study of superconductivity. In 1985, Bednorz and Müller [1] turned to study compounds of copper oxides. Among them, lanthanum and barium copper oxides with metallic conductivity were known. On varying the ratio La^{3+} to Ba^{2+} in these compounds, it was easy to control the valence of copper and the concentration of carriers. In January 1986 when performing measurements of conductivity in compounds with various concentrations of barium, Bednorz and Müller discovered a dramatic fall of the resistivity in some samples at temperatures below 35 K. The results of the measurements were published in the September issue of Zeitschrift fuür Physik [Bednorz and Müller, 1986]. The final confirmation of the superconducting nature of the phase transition in these samples was obtained after a verification of the Meissner effect [Bednorz et al., 1987]. The publication of this discovery attracted the attention of many scientists who, in a short period of time, confirmed the occurrence of superconductivity in the ceramics $La - M - Cu - O$, where M = Ba, Sr, Ca [Bednorz and Müller, 1988]. Later on, it became clear that the oxide superconductors of this type have a layered perovskite structure $La_{2-x}M_xCuO_4$ (LMCO).

Despite the great diversity of the cuprate superconductor compounds, they have a common structural element: the CuO_2 planes. It is generally believed that the high values of superconducting T_C and the anomalous normal state physical properties of cuprate materials are determined by the unique electronic structure of the CuO_2 plane (Figure 2.1).

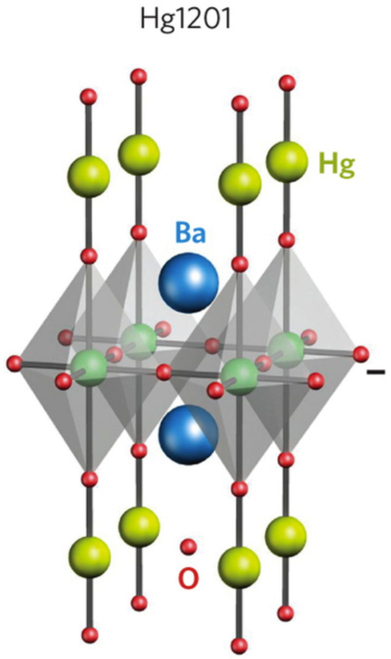

Figure 2.1: CuO_2 plane in the primitive cell of Hg1201. The grey shadow identifies the CuO_6 octahedra. The Cu atoms (green) together with the oxygens (red) forms the CuO_2 [Barisic et al., 2013].

[1] research associates at the IBM Research Division, Zürich Research Laboratory who were awarded the Nobel Prize in Physics in 1987

2.1 Electronic Structure CuO

In discussing the electronic structure of theCuO_2 plane, the crystal field splitting of the copper $3d$ levels and oxygen $2p$ levels is to be taken into account. In Figure 2.2 taken from [Plakida, 2010] there is a schematic outline of the formation of the in-plane electronic structure of CuO_2.   In a crystal field of cubic symmetry O_h, for a proper

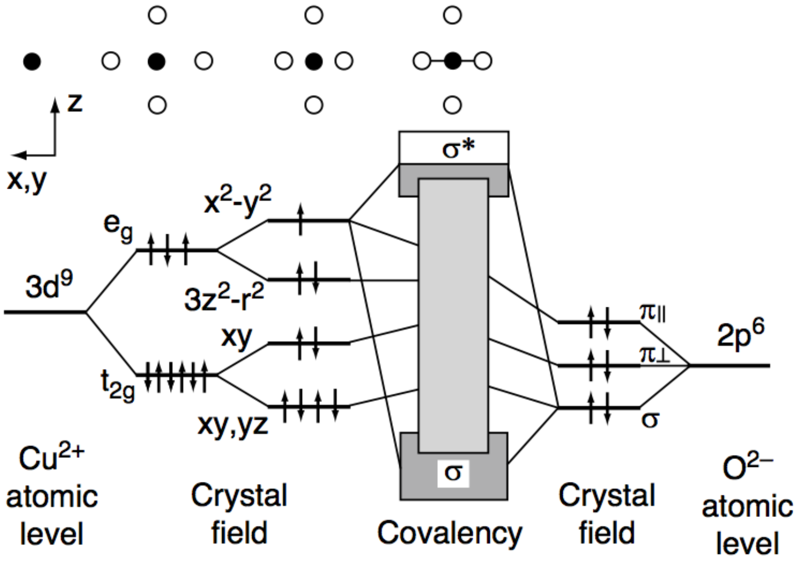

Figure 2.2: Formation of the electronic structure in CuO_2 planes, including the splitting of $3d$ and $2p$ levels in the crystal field and their covalent bonding.

octahedron CuO_6, the five $3d$ levels split into a doublet $e_g = \{d(x^2 - y^2), d(3z^2 - r^2)\}$ and a triplet $t_{2g} = \{d(xy), d(xz), d(yz)\}$. The value of this splitting is 1-2 eV [Bednorz and Müller, 1990]. Upon the decrease of symmetry to tetragonal D_{4h}, a further splitting of the $3d$ levels into singlets $b_{1g} = \{d(x^2 - y^2)\}, a_{1g} = \{(3z^2 - r^2)\}, b_{2g} = \{d(xy)\}$ and a doublet $e_g = \{d(xz), d(yz)\}$ occurs. The degenerate atomic $2p$ oxygen levels $p(x)$, $p(y)$, and $p(z)$ split in the crystal field of D_{2h} site symmetry into three levels: $(p\pi\|)$, $(p\pi\perp)$ and $(p\sigma)$. The π-type states correspond to the in-plane orbitals $p(x)$ or $p(y)$ $(\pi\|)$, or to the out-of-plane states $p(z)$ $(\pi\perp)$, which are directed perpendicular to the Cu-O bonds. The hybridization of the π-type states with the Cu orbitals is weak. This results in narrow π-bands. The σ-type states are formed by the oxygen in-plane orbitals $p(x)$ or $p(y)$, which are directed along the Cu-O bonds and the $d(x^2 - y^2)$ copper orbital. The linear combination of the four oxygen σ-type orbitals of the b_{1g} symmetry around a copper site experiences the strongest covalent bonding with the $d(x^2 - y^2)$ copper orbital which gives rise to broad bonding (σ) and antibonding $(\sigma*)$ bands of hybridized $pd\sigma$-states.

The other configuration of the four oxygen σ-type orbitals of a_{1g} symmetry does not couple to the copper $d(x^2 - y^2)$ orbital and results in a narrow nonbonding oxygen band. The three σ-type bonding configuration in the CuO_2 plaquette are shown schematically in Figure 2.3 [Damascelli et al., 2003]. The shaded and empty lobes of the $Cud(x^2 - y^2)$ orbitals and the in-plane $O_2p(x, y)$ orbitals denote the phases (positive and negative) of the wave functions.

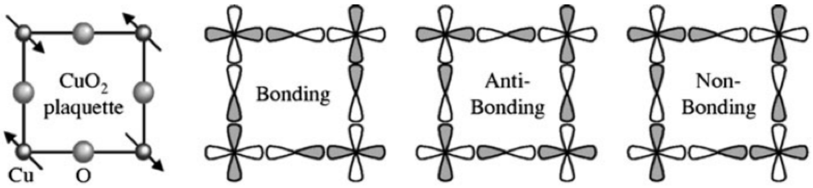

Figure 2.3: Formation of the electronic structure in CuO_2 planes, including the splitting of $3d$ and $2p$ levels in the crystal field and their covalent bonding.

From the picture of the formation of the electronic structure sketched in Figure 2.2, it follows that according to the band theory, this compound should be a metal with a half-filled antibonding $pd\sigma$ band. However, these conclusions contradict the experiments, which demonstrate that the cuprates compounds are antiferromagnetic insulators with a moderately wide energy gap of 1-2 eV. This discrepancy is related to the fact that, in the band scheme described, one neglects the Coulomb single-site repulsion of the $3d$ electrons. As already mentioned, the typical value of the Coulomb correlation energy is $U \sim 8 - 10$ eV. This is much larger than the typical width of the $pd\sigma$ antibonding band $W \sim 3$ eV, thus leading to the splitting of this band into two subbands. As we have seen, this is taken into account by the Hubbard model where the charge fluctuations of the type $d_i^n d_j^n \longrightarrow d_i^{n-1} d_j^{n+1}$ between two d_i^n ions of charges n at lattice sites i, j, involve the large d-d Coulomb interaction $U > W$. In the Mott-Hubbard model, it is also assumed that the Hubbard U that separates the LHB and the UHB is smaller than the energy gap Δ_{pd} that is necessary to transfer an electron from the $2p$ orbitals of the Oxigen to the $3d$ orbitals of the Copper. Therefore, the $2p$ orbital can be neglected if one considers only the narrow d band with a direct d-d exchange. However, the opposite situation, $U > \Delta_{pd} > W$, is also possible. In that case, the insulator correlation gap is defined by the energy of the charge transfer Δ_{pd} of the type: $d_i^n \longrightarrow d_i^{n+1} + 1h$ where h denotes a hole in the $2p$ Oxygen band. This type of insulator was called *charge-transfer insulator* [Zaanen et al., 1985]. It is just this situation which is realized in cuprates where the charge transfer energy $\Delta_{pd} = E_p - E_d \simeq 3 - 4$ eV is smaller than the correlation energy $U \simeq 8 - 10$ eV and therefore the copper oxide materials belong to the class of the charge-transfer insulators. The different types of electronic structures discussed above are illustrated in Figure 2.4 [Damascelli et al., 2003]. For a *p*-*d* model with three bands, bonding (B), nonbonding (NB) and the half-filled antibonding (AB) band, the following type of electronic structure can be realized, depending on the Coulomb repulsion U at the *d*-site, the charge-transfer gap Δ_{pd} and the hybridization bandwidth W: (a) a metallic state of AB band for $U = 0$, (b) a Mott-Hubbard insulator for $\Delta_{pd} > U > W$, (c) a charge-transfer insulator for $U > \Delta_{pd} > W$. If one takes into account the strong *d*-*d* correlations and the *p*-*d* hybridization for two-hole states in the CuO2 plaquette, then the two-hole *p*-*d* band splits into a triplet ($S = 1$) and a singlet ($S = 0$) bands [Zhang and Rice, 1988] (d).

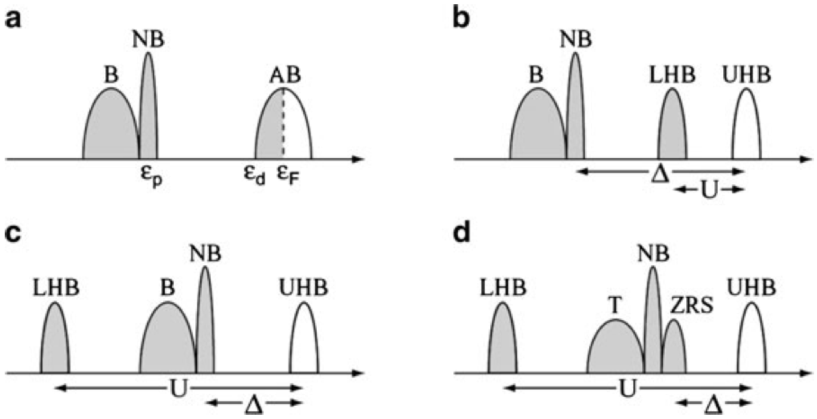

Figure 2.4: Illustration of the electronic structure of the *p*-*d* model with three bands, bonding (B), nonbonding (NB), and antibonding (AB): (a) a metallic state at half-filling of AB band for$U = 0$, (b) a Mott-Hubbard insulator for $\Delta > U > W$, (c) a charge-transfer insulator for$U > \Delta > W$, and (d) the same as (c) but with the two-hole *p*-*d* band splitted into the triplet (T,S=1) and the Zhang-Rice singlet (ZRS, S=0) bands

2.2 *Cuprate Phase Diagram*

A schematic phase diagram of the cuprates is shown in Figure 2.5 ([**?**]). Here, the x-axis is a material property, the doping level, which controls the electron concentration per copper site in the all important Cu-O planes, and the y-axis is the temperature, T. The unprecedentedly high T_C and the intimate relation between superconductivity and antiferromagnetism are only two of the unexpected features of this phase diagram. At very low levels of hole doping, cuprates are insulating and antiferromagnetic (the materials' neighbouring spins point in opposite directions). At increased doping levels, they become conducting, and the exact temperature and doping level determine which phase of matter they will be in. At temperatures below T_C, they become superconducting, and at temperatures above T_C but below T^* they fall into the pseudogap phase. The boundary of the pseudogap region at low doping levels is unknown. The transition between the Fermi-liquid phase and the strange-metal phase occurs gradually (by crossover). QCP denotes the quantum critical point at which the temperature T^* goes to absolute zero.

- The origin and character of the antiferromagnetic state which is the ”parent” of the high temperature superconductors is well understood from the strong-coupling perspective in which the insulating character derives from the classical repulsion U between two electrons on the same atom, and the antiferromagnetism from the superexchange interaction J.

- Various attempts to obtain a semiquantitative estimate of the superconducting transition temperature T_C, have had some measure of success [Dahm et al., 2009], but certainly, there has not yet been any salient success in the theoretical prediction of new high temperature superconductors, or even in predicting which small changes to existing materials would produce increases (or decreases) in T_C. Recent developments in numerical methods for handling the physics of strongly interacting electrons from short to intermediate length scales [Stoudenmire and White, 2012], coupled with new ways of preparing and manipulating copper-oxide materials [Gozar et al., 2008].

- A conventional superconductor has the same symmetries as the underlying crystal, while in the cuprates it has *d*-wave symmetry [Tsuei and Kirtley, 2000], which means that the superconducting wavefunction changes sign upon rotation by 90 degrees. Associated with this unconventional pairing is the existence of zero energy (gapless) quasiparticle excitations at the lowest temperatures, which make even the thermodynamic properties entirely distinct from those of conventional superconductors which are fully gapped. The reasons for this, and its relation to a proximate antiferromagnetic phase, are now well understood, and indeed were anticipated early on by some theories[Scalapino et al., 1986].

- The state at temperatures just above T_C, out of which the superconducting state condenses, is in most cases the *pseudogap* which is characterized by a substantial suppression of the electronic density of states at low energies that cannot be simply related to the occurrence of any form of broken symmetry. While much about this regime is still unclear, increasingly clear experimental evidence has recently emerged that there are strong and ubiquitous tendencies toward several sorts of order or incipient order, including various forms of charge density wave (CDW), spin density wave (SDW), and electron nematic order, and possibly pair-density wave (PDW) and orbital loop current (OLC) order, all of which compete with uniform *d*-wave superconductivity and exhibit similar energy scales. There are many fascinating aspects of these ”intertwined orders” that remain to be understood.

- The fact that at temperatures well above T_C, the conductivity is almost two orders of magnitude smaller than in simple metals and exhibits frequency and temperature dependences that are incompatible with the conventional theory of metals has led to this regime being referred to as a ”strange metal” or ”bad metal”. The exhibited behavior, which is simple to describe in terms of the so-called ”marginal Fermi liquid phenomenology” [Varma et al., 1989], has resisted any generally accepted understanding. On the other hand, similar behavior has now been documented in a large number of electronically interesting materials, indicating that this is a general property of strongly correlated electron systems, and not directly linked to high temperature superconductivity. This can be considered the most significant open problem in the understanding of quantum materials.

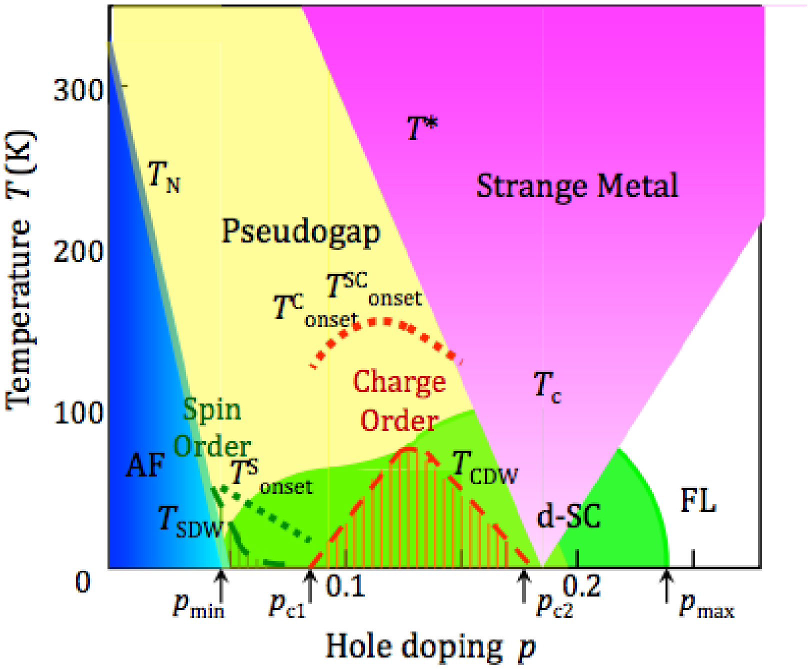

Figure 2.5: Temperature versus hole doping level for cuprates, indicating where various phases occur. AF is antiferromagnet, d-SC d-wave superconductivity, and FL Fermi liquid. SDW and CDW represent incommensurate spin density wave and charge density wave order. Onset marks where precursor order or fluctuations become apparent ([**?**]).

2.3 Pseudogap Phase

(Figura fermi arcs) What has emerged in recent years about the pseudogap phase is that a variety of orders different from superconductivity are at play here. Some involve ”crystallization” of the electrons, in the form of stripes and other forms of charge order, but others appear to be more novel quantum liquids. In the underdoped regime, the doped holes remain mobile even at low temperatures, but organize themselves collectively. All these kinds of organization lye below a line called T^* which denotes the onset of a partial gap observed in spectroscopic data.

The first evidence of a pseudogap regime comes from NMR measurements which showed a reduction in the low-frequency spin excitations [Warren et al., 1989]. This pseudogap was subsequently seen in c-axis polarized infrared conductivity measurements associated with a pronunced upturn of the c-axis resistivity [Homes et al., 1993] together with a reduction of the in-plane resistivity [Ito et al., 1993] [Puchkov et al., 1996].

The idea that this could be related to forms of order other than pairing was brought to light by the experimental discovery of electronic ”stripes” in the LSCO family [Tranquada et al., 1995]. This was inspired by earlier theoretical work that discovered that the mean field solution for doped Mott insulators on a square lattice in the intermediate coupling regime consists of Mott-insulating antiferromagnetic domains, separated by a regular ”stripe” array of antiferromagnetic domain walls trapping the doped holes [Zaanen and Gunnarsson, 1989].

Quite recently, evidence has emerged that materials with static stripes form a pair density wave: the charge stripes are internally superconducting, with a phase that reverses from stripe to stripe. Given that, the stripe orientation changes as one moves from one layer to the next, this frustrates the Josephson coupling between layers, giving rise to a two dimensional superconducting state [Tajima et al., 2001].

In a parallel development, the structure of the pseudogap in momentum space was directly mapped by ARPES, showing that this mimics the d-wave superconducting gap: a gap was apparent only in the ”antinodal” regions of the Brillouin zone [Marshall et al., 1996] [Ding et al., 1996] [Loeser et al., 1996]. The character of these observations is best illustrated by showing a map of the spectral weight at low energy as a function of **k** in the first Brillouin zone (Figure 2.6). In a Fermi liquid, the Fermi surface delineates the boundary between occupied and unoccupied quasiparticle states, so no matter how complicated it may be, the one thing it cannot do is abruptly end.

However, in the pseudogap regime, there appear to be ”Fermi arcs” in the nodal regime [Norman et al., 1998]. In a mean-field theory, the effective potential associated with a (density-wave) state that breaks translational symmetry can reconstruct a large Fermi surface, producing small Fermi surface pockets, but these still have to form connected manifolds. It is plausible that the Fermi arcs are actually the front half of such a pocket [Marshall et al., 1996] and hence there has been an intense search to find the ”backside of the pocket”. As a function of decreasing temperature a BCS-like gap opens on the arc eventually merging with the antinodal gap into an overall gap structure that, at low temperatures, is not all that different from a simple BCS d-wave gap. In lightly doped cuprates the Fermi surface that is present in the overdoped, more conventional Fermi liquid regime is destroyed, leaving behind only a Fermi arc [Norman et al., 1998]. The suggestion was immediate that already at the very high pseudogap temperature T^*, pairs start to form while phase fluctuations prohibit superconducting order until much lower temperatures (see Figure 2.6). The best evidence of a pairing correlations without substantial phase coherence persisting to temperatures of order T^* is in the temperature evolution of the gap itself as shown by [Renner et al., 1998] in Figure 2.7 where tunnelling measurements on Bi-2212 underdoped sample are shown. It is possible to see that the sharp coherence peaks observed at low temperatures diminish as the temperature increases and above T_C transform to broad maxima. The

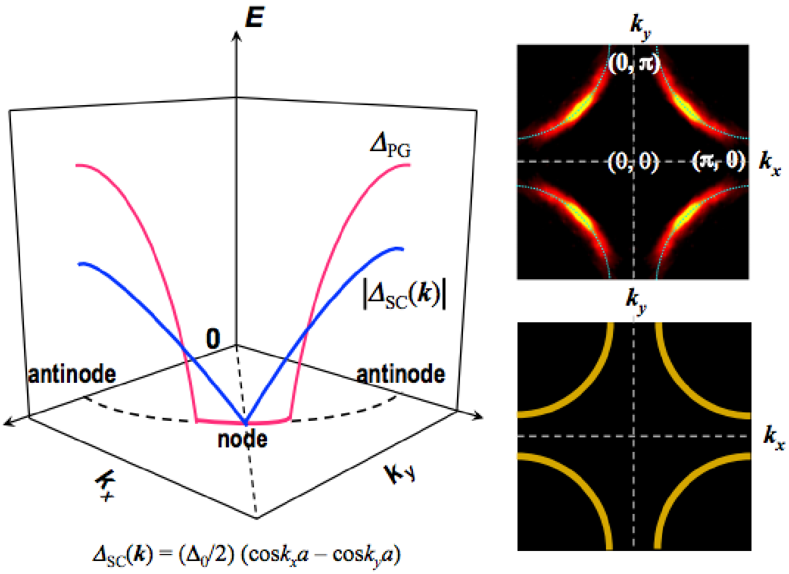

Figure 2.6: Fermi surface, Fermi arcs, and gap functions. The large Fermi surface predicted by band theory is observed by ARPES and STS for overdoped compounds (bottom right). But once the pseudogap sets in, the antinodal regions of the Fermi surface are gapped out, giving rise to Fermi arcs (top right). This is reflected (left) in the angle dependence of the superconducting gap (SC) and pseudogap (PG) around the underlying large Fermi surface (dashed curve) as revealed by ARPES and STS. Note the gapless region around the *d*-wave superconducting node for the PG case that defines the Fermi arcs. These arcs appear to be reconstructed into electron pockets centered at $(Q/2, Q/2)$ once charge order sets in, as revealed by quantum oscillation studies, where $(Q, 0)$ is the charge order wavevector.

dip structure characteristic to the superconducting state vanishes above T_C also. Thus, the superconducting gap evolves continuously into a normal state pseudogap above T_C. With further increase of the temperature, the pseudogap is filling up by excitations. Yet another interesting hint regarding the unusual relationship between the charge order and superconductivity follows from the temperature evolution of the charge order. The X-ray signal begins to build up smoothly upon cooling below some T_{CDW} typically less than T^* to attain a maximum at the superconducting T_C, then drops significantly below T_C, indicating competition between the CDW order and superconductivity [Ghiringhelli et al., 2012] [Chang et al., 2012]. Moreover there is evidence of the onset of a small Kerr rotation at T^* which also indicates some type of symmetry breaking [Xia et al., 2008]. This Kerr signal defines a phase line that cuts through the superconducting dome, vanishing near 18% doping.

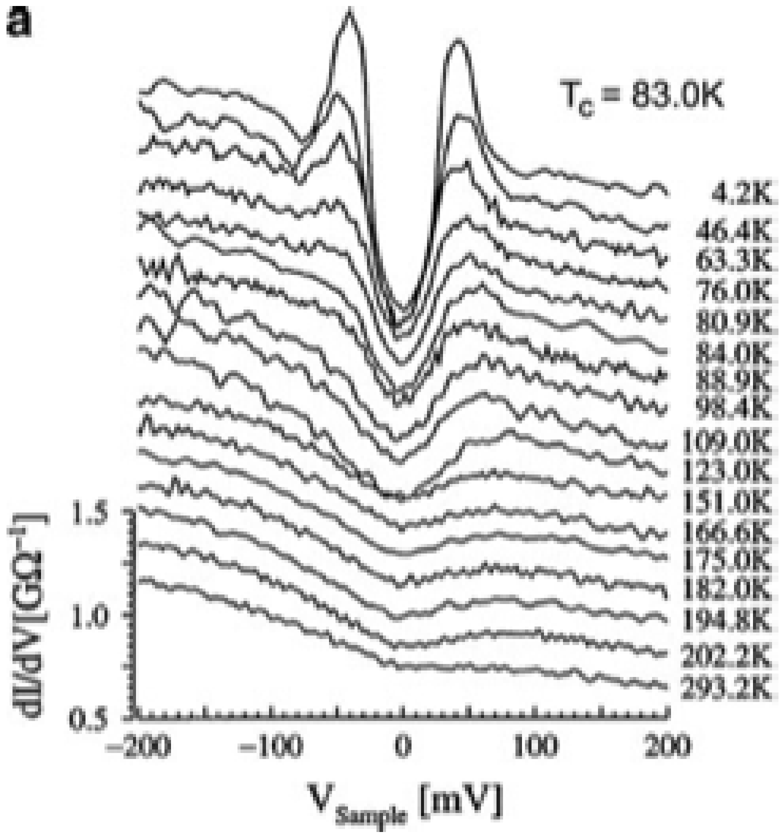

Figure 2.7: Tunneling spectra measured as a function of temperature on underdoped Bi2212. The conductance scale corresponds to the 293 K spectrum, the other spectra are offset vertically for clarity.

In conclusion the pseudogap regime is characterized by a plethora of orders that are still far to be completely understood. Away from the ordered states, things become even more mysterious and we get into a phase called ”strange metal phase”.

2.4 Non-Fermi liquid Phase and Quantum Criticality

The gross difference of the strange metal phase from that of conventional metals is the absence of quasiparticles. This has consequences for simple physical properties like the electrical resistivity. In a normal metal, the resistivity saturates at high temperatures when the mean free path becomes of order the electron de Broglie wavelength. The resistivity of the cuprate strange metal can be linear in T from near T_C up to as high a temperature as measured [Martin et al., 1990], in contrast to the T^2 dependence predicted by the Landau Fermi-liquid theory (See the phase diagram in Figure 2.8 taken from [Hussey, 2008]). Moreover, the Hall resistivity has a different temperature dependence than would be expected in a quasiparticle picture [Chien et al.].

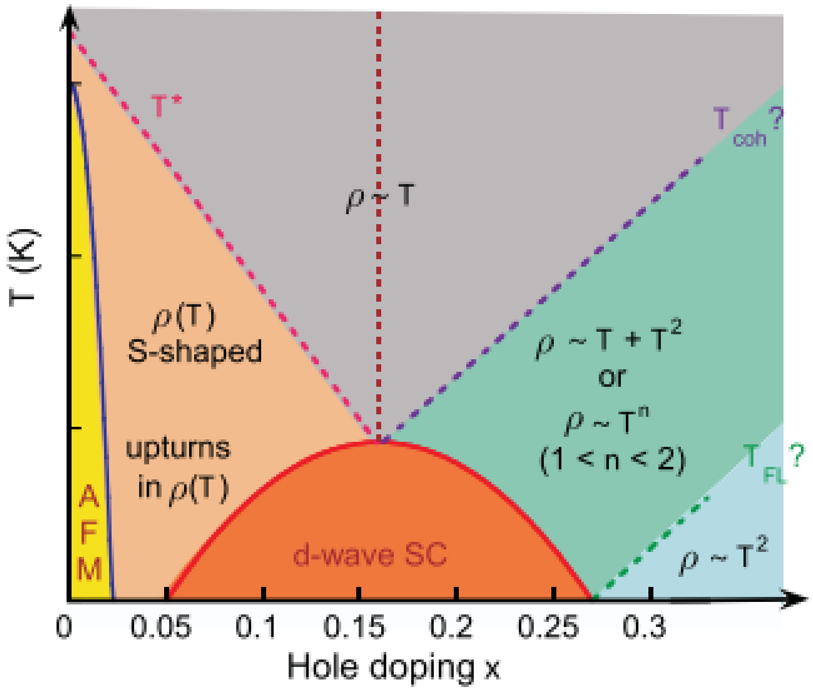

Figure 2.8: Crossover phase diagram for the resistivity (ρ) in the hole doped cuprates. The strange metal phase is the regime above optimal doping where $\rho \propto T$.

In the 1990s the idea of quantum criticality emerged to explain the low energy excitations of the strange metal. A quantum phase transition occurs when a continuous phase transition occurs at zero temperature as a function of a tuning parameter (like pressure or doping), where the corresponding quantum critical point (QCP) defines the boundary between the ordered (broken symmetry) and disordered quantum phases [Sachdev, 2001]. There is a quantum critical wedge opening up from the QCP. This gives a suggestive interpretation of the phase diagram in Figure 2.5, where the strange metal is identified with the quantum critical wedge associated with a QCP under the superconducting dome near optimal doping. The theory of quantum criticality in metallic systems is still a work in progress. One issue is that there may be reasons to believe that the QCP is intrinsically unstable, since the order parameter fluctuations mediate attractive interactions that promote superconductivity, meaning that the quantum critical point might always be ”shielded” by a superconducting dome, just as in Figure 2.5. Moreover, according to the marginal Fermi liquid phenomenology [Varma et al., 1989], what is needed is a rather special sort of quantum criticality that is local in space, and so featureless in **k**. Is there a quantum critical point involving the termination of pseudogap order inside the superconducting dome? There is evidence for this to be the case, early on from specific heat data [Tallon et al., 1994] and more recently from a Fermi velocity anomaly seen in photoemission [Vishik et al., 2012]. But which order parameter rules the quantum critical regime, and is that regime large enough to encompass the entire strange metal region? The pseudogap is characterized by several competing ordering tendencies. Even more seriously, this quantum critical description should break down at higher (ultraviolet) temperatures. How to explain then that the resistivity stays linear in T up to temperatures where the crystal melts?

3 Optical Spectroscopy at equilibrium

Interaction between light and matter is the base of the spectroscopy techniques. Usually, the description of the electrodynamics of metals and superconductors is uniquely defined by the complex *dielectric constant* $\epsilon(\omega) = \epsilon_1(\omega) + i\epsilon_2(\omega)$ and the complex *optical conductivity* $\sigma(\omega) = \sigma_1(\omega) + i\sigma_2(\omega)$. The real and imaginary part of these two constant are related by $\sigma_1(\omega) = (\frac{\omega}{4\pi})\epsilon_2(\omega)$ and $\sigma_2(\omega) = -(\frac{\omega}{4\pi})[\epsilon_1(\omega) - 1]$. The reflectivity $R(\omega)$ and transmittivity $T(\omega)$ of a material are uniquely described by these optical constants:

$$R(\omega) = \left| \frac{1 - \sqrt{\epsilon(\omega)}}{1 + \sqrt{\epsilon(\omega)}} \right|^2 \tag{3.1}$$

By the fact that the real and imaginary part of the optical constants are linked together by the Kramers-Kroning (KK) relations, one can infer both these parts by the analysis of the raw transmittivity and reflectivity data of a sample.

3.1 Drude Lorentz Model

The electromagnetic energy is absorbed and dissipated in a solid through multiple channels, with a rate that is proportional to the imaginary part of the dielectric constant (or equivalently the real part of the optical conductivity) $W = \frac{\omega\epsilon_2(\omega)}{4\pi}E^2 = 2\sigma_1(\omega)E^2$. A classical model to describe the various excitations of radiations in a solid is the *Drude-Lorentz oscillator model*:

$$\sigma(\omega) = \frac{1}{4\pi}\frac{\omega_{pD}^2}{1/\tau_D - i\omega} + \frac{\omega}{4\pi}\sum_j \frac{\omega_{pj}^2}{\omega/\tau_j - i(\omega^2 - \omega_j^2)} \tag{3.2}$$

The first term refers to the relaxation of the free charge carriers with the scattering rate $\gamma = 1/\tau_D$; the second term is a sum of Lorentz oscillators - characterized by the central frequency ω_j, the strength of the oscillator ω_{pj}^2 and the scattering rate $\gamma_j = 1/\tau_j$ - that describe the response of bound charges (Figure 3.1).

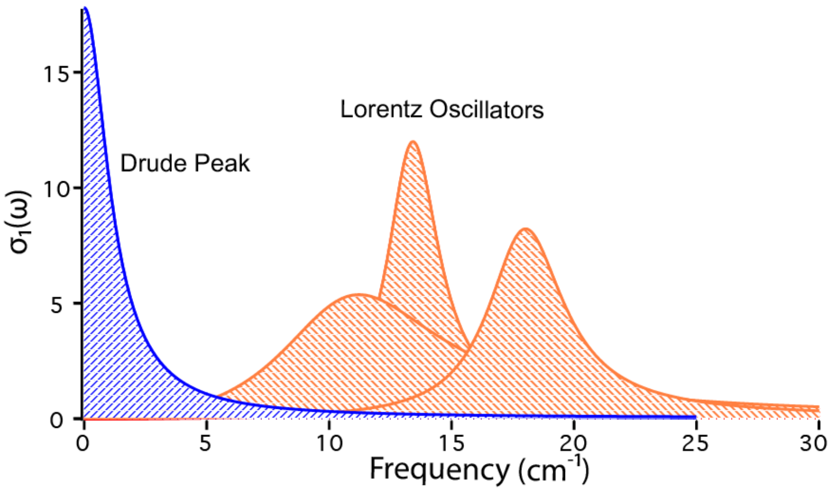

Figure 3.1: Modellization of the Optical Conductivity with the Drude-Lorentz model.

3.2 *Extended Drude Model*

The Drude model describes the optical conductivity of a gas of non-interacting electrons with a single, energy independent channel of dissipation: $4\pi\sigma(\omega) = \omega_p^2/(1 - i\omega\tau)$. This model is insufficient to describe the situation where the dissipation in the electron system arises from the electron-phonon or electron-electron interactions. To account for the life-time dependence on the frequency and the renormalization of mass of free carriers due to many-body effects, the *extended Drude model* is frequently used and the optical conductivity writes:

$$\sigma(\omega) = \frac{1}{4\pi}\frac{m}{m^*(\omega)}\frac{\omega_p^2}{1/\tau^*(\omega) - i\omega} \tag{3.3}$$

where $m^*(\omega)$ is the renormalized mass and $1/\tau^*(\omega) = (m/m^*(\omega))(1/\tau(\omega))$ is the renormalized scattering rate. The previous formula can be written using the *memory function*:

$$\sigma(\omega) = \frac{1}{4\pi}\frac{i\omega_p^2}{\omega + M(\omega)} \tag{3.4}$$

where $M(\omega)$ is defined as:

$$M(\omega) = \omega\lambda(\omega) + i\Gamma(\omega) \tag{3.5}$$

The memory function is a complex function $M(\omega) = M'(\omega) + iM''(\omega)$ which determines the renormalized optic mass $m^*(\omega)/m(\omega) = 1 + \lambda(\omega)$ and the renormalized scattering rate $1/\tau(\omega) = \Gamma(\omega)$. These two functions are KK related:

$$\lambda(\omega) = \frac{2}{\pi}P\int_0^\infty \frac{\Gamma(z)\,\mathrm{d}z}{z^2 - \omega^2} \tag{3.6}$$

The renormalized transport life time equals to $\tau^*(\omega) = \tau(\omega)[1 + \lambda(\omega)]$ and these parameters are expressed in term of the real and imaginary part of the inverse conductivity:

$$\frac{1}{\tau(\omega)} = \frac{\omega_p^2}{4\pi}\mathrm{Re}\frac{1}{\sigma(\omega)} \;; \qquad \frac{m^*(\omega)}{m} = 1 + \lambda(\omega) = -\frac{\omega_p^2}{4\pi}\mathrm{Im}\frac{1}{\sigma(\omega)} \quad (3.7)$$

Two related quantities are the effective mass, $m^*(\omega)/m = M'(\omega)/\omega + 1$ and scattering rate, $1/\tau(\omega) = M''(\omega)$. These quantities are useful because they are more easily interpreted physically.

The real part of the memory function (3.5) is a frequency dependent scattering rate due to the electron-phonon scattering (in the Drude model the inelastic impurity scattering makes the scattering rate a constant), while the imaginary part $\lambda(\omega)$ is related to the renormalization of the electronic effective mass due to the strong correlations [Basov and Timusk, 2005]. The memory function $M(\omega)$ has the same analytical properties of the one-particle self energy $\Sigma(\omega)$ (averaged over the Fermi surface) used in the Green function theory, but conceptually it is a different quantity. $\Sigma(\omega)$ is directly measured by a photoemission experiment, since this technique probes the single particle excitations of the $(N-1)$ particle system, which can be described in terms of the spectral function and the single particle self energy. An optical experiment, instead, looks at the particle-hole excitations of an $N-$particle system and gives information about the joint particle-hole density of states. In the so-called Allen approximation [Allen, 1971], $M(\omega)$ can be write as a convolution integral between a transport spectral function $\alpha_{tr}^2 F(\Omega)$ and a kernel function $K(\frac{\omega}{2\pi T}, \frac{\Omega}{2\pi T})$ which describes the thermal dependence of the phononic excitations coupled with electrons.

$$M(\omega) = \int_0^\infty \alpha_{tr}^2 F(\Omega) K(\frac{\omega}{2\pi T}, \frac{\Omega}{2\pi T}) \quad (3.8)$$

where

$$K(x,y) = \frac{i}{y} + \left\{ \frac{y-x}{x}[\Psi(1-ix+iy) - \Psi(1+iy)] \right\} - \{y \to -y\} \quad (3.9)$$

where $\Psi(x)$ is the Digamma function. An interesting method to determine $\alpha_{tr}^2 F(\Omega)$ directly from the raw data was found by [Marsiglio and Carbotte, 2001] and it is based on the second derivative of the conductivity with respect to the frequency:

$$\alpha_{tr}^2 F(\Omega) = \frac{1}{2\pi}\frac{\omega_p^2}{4\pi}\frac{d^2}{d\omega^2} Re\left(\frac{1}{\sigma(\omega)}\right) \quad (3.10)$$

The microscopic derivation of the complex conductivity $\sigma(\omega)$ in the presence of strong electron-phonon correlations is achieved starting from the Kubo formula and using complex diagrammatic techniques to evaluate the electron and phonon Green functions. Omitting the vertex corrections (Migdal approximation) it is possible to simplify the calculations and to obtain an expression of $\sigma(\omega)$ in terms of the one-particle self-energy function:

$$\sigma(\omega,T)=\frac{i\omega_p^2}{4\pi\omega}\int_{-\infty}^{+\infty}\frac{f(\omega+\epsilon,T)-f(\epsilon,T)}{\omega-\Sigma(\omega+\epsilon,T)+\Sigma^*(\epsilon,T)+i\Gamma_{imp}} \tag{3.11}$$

where $f(\epsilon,T)$ are Fermi factors and $\Sigma(\omega)$ and $\Sigma^*(\omega)$ are self-energies above and below the Fermi energy. Under some assumptions[1] we can express the single particle self-energy as

$$\Sigma(\omega,T)=\int d\epsilon\int d\omega'\Pi(\omega')\left[\frac{n(\omega')+f(\epsilon)}{\omega-\epsilon+\omega'+i\delta}+\frac{n(\omega')+1-f(\epsilon)}{\omega-\epsilon-\omega'-i\delta}\right] \tag{3.12}$$

where $n(\epsilon,T)$ is the Bose function and $\Pi(\omega)$ is the so called *glue function*. A general function of $\Pi(\omega)$ consists of a histogram representation using N blocks with adjustable positions and heights:

$$\Pi(\omega)=f_i \qquad \omega_{i-1}\leqslant\omega\leqslant\omega_i \tag{3.13}$$

where i runs from 1 to N, $\omega_0=0$ and f_i is the height of the block. For cuprates the function $\Pi(\omega)$ consists of two main features: a peak with an energy in the range $50-60$ meV and a broad spectrum extending up to 400 meV [van Heumen, 2009].

3.3 Spectral Weight

The optical constants of solids obey a variety of sum rules (Smith, 1998). The origins of the sum rules can be traced back to fundamental conservation laws and are intimately connected to the causality of the electromagnetic response. Analysis of the sum rules is a powerful tool that can be used to study the distribution of the spectral weight (SW) in correlated electron systems because they indicate conserved quantities, that is, quantities that do no change under a change, for example, of temperature. Of special practical importance is the *global oscillator strength sum rule* relating the integral of the dissipative part of the optical conductivity to the density of particles participating in optical absorption and their bare mass:

$$SW=\int\limits_0^\infty\sigma_1(\omega)\mathrm{d}\omega=\frac{\pi ne^2}{2m_e}=\frac{1}{8}\omega_p^2 \tag{3.14}$$

The optical conductivity of a metal is dominated by the electronic response and therefore an integration of the data using the previous formula can be compared to the total number of electrons, including

[1] a) neglect vertex corrections and the energy dependence of the density of states. b) the self-energies are assumed to be momentum independent.

both core and valence electrons. The integration to infinite frequency can rarely be exercised because of experimental constraints. In principle, nothing prevents spectral weight transfer to occur form one spectral region to another. To extract useful information, it is customary to consider a partial sum rule, calculating the spectral weight up to a cutoff frequency, ω_c. The partial spectral weight is defined as:

$$SW(\omega_c) = \int\limits_0^{\omega_c} \sigma_1(\omega) \mathrm{d}\omega = \frac{\pi N_{eff} e^2}{2m} \tag{3.15}$$

The natural cutoff frequency to be chosen, is the one at the crossover between intraband and interband contributions to the dielectric function. This energy cutoff equals $\sim$ 1 eV in cuprates, while it is smaller in conventional, BCS superconductors. For both the normal state and superconducting state spectral weight, one can thus write: $SW = A + B$ where:

$$A = \int\limits_0^{\omega_c} \sigma_1(\omega) \mathrm{d}\omega \ ; \qquad B = \int\limits_{\omega_c}^{\infty} \sigma_1(\omega) \mathrm{d}\omega \tag{3.16}$$

A represents the intraband contribution to the spectral weight, while B represents the interband contribution. The sum rule for band electrons is in practice the most useful. Suppose that we have a system with only a single reasonably well isolated band around the Fermi level that can be approximated by a tight binding dispersion $\epsilon_k = -t\cos(ka)$. In that case we find an interesting relation,

$$\int\limits_0^{\omega_c} \sigma_1(\omega, T) \mathrm{d}\omega = -\frac{\pi e^2 a^2}{2\hbar^2 V} \sum_{k,\sigma} \langle \hat{n}_{k\sigma} \epsilon_k \rangle_T = -\frac{\pi e^2 a^2}{2\hbar^2 V} E_{kin}(T) \tag{3.17}$$

This sum rule states that by measuring the optical spectral weight we are in fact measuring the kinetic energy of the charge carriers contributing to the optical conductivity. In real systems this relation only holds approximately: usually there are other bands lying nearby and the integral on the left contains contributions from these as well. Often the bands are described by more complicated dispersion relations in which case the relation $\partial^2 \epsilon_k / \partial k^2 = -\epsilon_k$ does not hold. We can make some other observations from the sum rule for band electrons. Suppose again we have a single empty cosine like band (it is only necessary that the band is symmetric but it simplifies the discussion) at $T = 0$. Since the band is empty, the spectral weight is equal to zero. If we start adding electrons the spectral weight starts to increase until we reach half-filling. If we add more electrons the spectral weight will start to decrease again because the second derivative becomes negative for $k > \pi/2a$. If we completely fill the band the contributions from $k > \pi/2a$ will precisely cancel the contributions from $k < \pi/2a$ and the spectral weight is again zero. Now consider what happens if we have a half-filled band and start to increase the temperature. Due to the smearing of the Fermi-Dirac distribution higher energy states will get occupied leaving behind lower energy empty states. The result of this is that the spectral weight starts to decrease. One can show using the Summerfeld expansion that the spectral weight follows a T^2 temperature dependence. In the extreme limit of $T \rightarrow \infty$ something remarkable happens: the Fermi-Dirac distribution is $1/2$ everywhere and the electrons are equally spread out over the band. The metal has become an insulator.

3.4 Temperature and Doping Dependence of Cuprates Optical Properties

Studies of frequency dependence of infrared reflection on single crystals and films of the cuprate superconductors have provided, complementary to the ARPES studies, information on transition from a charge-transfer insulator to a metallic state under hole or electron doping. In Figure 3.2 there is the doping dependence of the optical conductivity $\sigma_1(\omega)$ of $La_{2-x}Sr_xCuO_4$ and $Nd_{2-x}Ce_xCuO_{4-y}$ samples [Uchida et al., 1991]. In the insulator phase ($x = 0$), absorption appears only at photon energies $\hbar\omega < 1$ eV, which indicates the existence of the insulator optical gap at $\hbar\omega \sim 1.5$ eV. In accordance with the general structure of the electronic spectrum shown in Figure 2.4, this gap is caused by a charge transfer from the filled O $2p$-type band to the upper Hubbard Cu $3d$ subband. Under doping (hole doping-type in LSCO and electron doping-type in NCCO compounds), the intensity of this absorption decreases, but there appears an absorption in the mid-infrared (MIR) region,

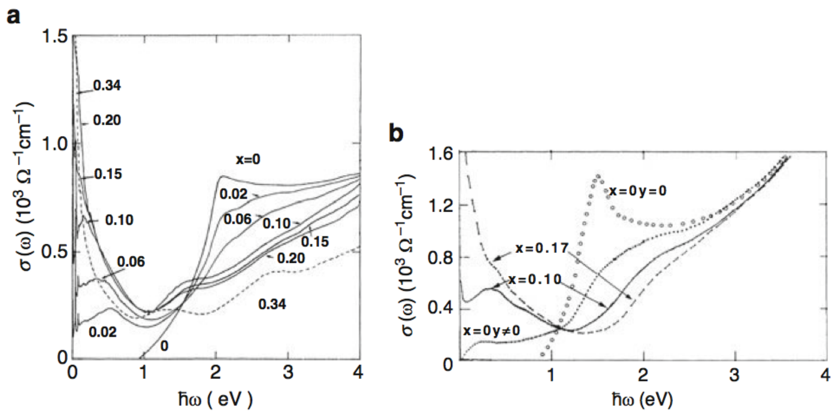

Figure 3.2: Optical conductivity $\sigma_1(\omega)$ of $La_{2-x}Sr_xCuO_4$ (a) and of $Nd_{2-x}Ce_xCuO_{4-y}$ (b) as a function of doping

$\hbar\omega < 1$ eV, which increases more rapidly than the concentration of carriers. An absorption characteristic of metals in the form of Drude peak in Figure 3.1 also appears near $\omega = 0$. These results suggest a spectral weight transfer from the upper Hubbard band to the *p*-*d* singlet states under hole doping. A strong dependence of the optical conductivity on doping, as shown in Figure 2.4, was obtained only for the absorption in the CuO_2 plane; for the polarization of light out of the plane the absorption spectrum preserves its insulator nature even in the overdoped region [Uchida et al., 1996].

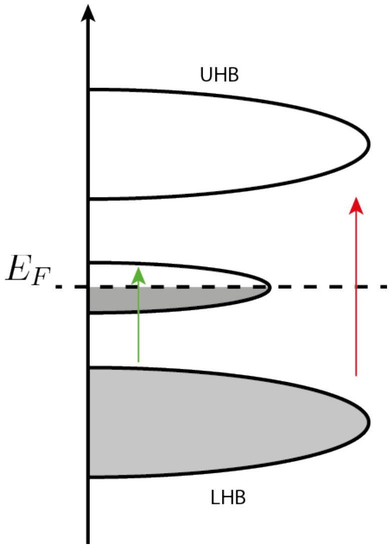

Figure 3.3: Schematic global density of states of hole-doped Mott insulators. The band around the Fermi level, the upper Hubbard band (UHB), and the lower Hubbard band (LHB) are schematically illustrated. The red arrow represents the charge-transfer excitation, the green arrow identifies the excitations in the mid-IR region.

According to exact diagonalization calculations for the Hubbard model [Nakano et al., 2007] At low doping $p < 0.1$, a quick grows of the MIR incoherent part of the conductivity spectrum occurred due to the spectral weight transfer from above the Mott gap, while the Drude weight increased as p^2. At larger doping, the MIR part did not change much and the further increase of the conductivity with doping was due to the Drude weight growth, which saturated at overdoping. A two-component description (3.2) in the underdoped region with the Drude-type component for coherent motion of doped holes at $\omega \sim 0$ and a broad component in the MIR region due to incoherent hole motion or the states created in the gap region (Figure 3.3). In the moderately doped region, $0.1 < p < 0.25$, the separation of the IR absorption into the Drude-type and MIR band becomes ambiguous and a description within the general Drude formula can be used. A detailed study of temperature and frequency dependence of the optical conductivity in a broad frequency range 30-20000 cm^{-1} [2] in several $YBa_2Cu_3O_{6+x}$ single crystals has be done in [Orenstein et al., 1990] revealed in the insulator sample $p = 0.2$ an optical gap, $\hbar\omega \simeq 1.75$ eV, determined by the energy of charge transfer $O_2p \rightarrow Cu_3d$. With an increase of the doping absorption appeared in the MIR region, accompanied by the Drude absorption peak at $\omega = 0$. These two regions were clearly separated by a strong suppression of $\sigma(\omega)$ at $\omega \sim 500$ cm^{-1} clearly seen at low temperatures, in the underdoped crystals even above T_C. The analysis of frequency and temperature dependence of $\sigma(\omega)$ at different concentrations of carriers have led to the conclusion that two components exist in the infrared absorption. A rather narrow Drude component in (3.2) with a typical width $\gamma \simeq k_B T$ affects only a small part of the effective number of free carriers participating in absorption. The second component is related to absorption in the MIR region, $k_B T < \hbar\omega < 1$ eV, whose intensity, like that of the Drude peak, rapidly increases with the number of doped carriers. A detailed analysis of the infrared conductivity in single crystals of $YBa_2Cu_3O_y$ for ten different doping levels, $6.28 < y < 7.00$, has been reported in [Lee et al., 2005] and shows the evolution of the infrared conductivity with doping from the antiferromagnetic (AF)

[2] 1 eV= 8064 cm^{-1}

phase in strongly underdoped region to the superconducting phase at optimal doping. The doping dependence of the optical spectra $\sigma_1(\omega)$ is shown in Figure 3.4. In the inset, the $\sigma_1(\omega)$ is shown up to the photon energy $\hbar\omega = 3.75$ eV, which demonstrates the charge-transfer gap at $\sim$ 1.5 eV. Two components are clearly seen in the conductivity at low temperature, a narrow Drude-like peak at the energies below $\sim$ 30 meV and a broad MIR band with a maximum, which decreases with doping. The effect of the temperature on these two components is to reduce the Drude peak at low temperatures with a strong temperature dependence, while the MIR absorption is essentially T-independent. This behavior is demonstrated in Figure 3.5 for two crystals: (a) $y = 6.35$ and (c) $y = 6.65$ where the two components are displayed by the dotted and dot-dashed lines in the left panels.

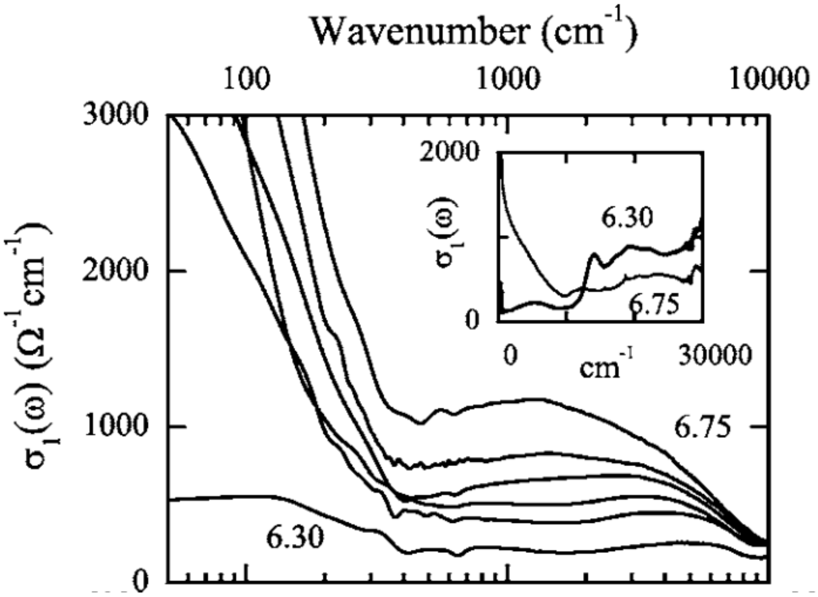

Figure 3.4: Optical conductivity $\sigma_1(\omega)$ of $YBa_2Cu_3O_y$ under various doping $6.30 < y < 6.75$

To see what happen to the charge-transfer spectrum around 2 eV we report in Figure 3.6 data taken by [Falck et al., 1992] on La_2CuO_4. We report just two measurements of the imaginary part of the dielectric function $\epsilon_2(\omega)$ for temperature at 122 K and 447 K. The charge-transfer peak around 2 eV is seen to sharpen and move to higher energies upon cooling. At $T \sim 120$ K this evolution saturates and further cooling alters neither the position nor the width of the peak. This behaviour can be described introducing a short-range interaction between electrons and holes that gives origin to a polaron. The temperature dependence of the polaron self-energy causes a shift

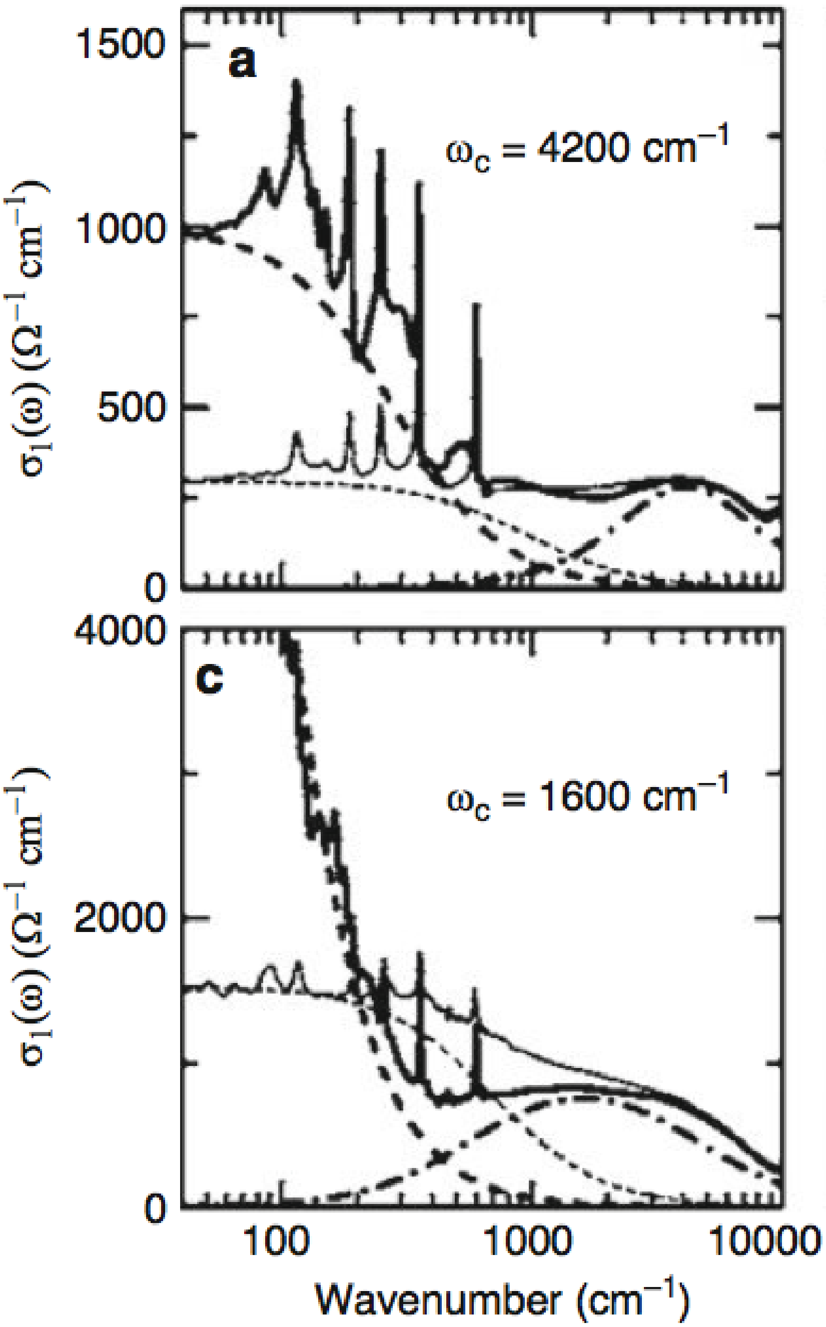

Figure 3.5: Optical conductivity $\sigma_1(\omega)$ of the $YBa_2Cu_3O_y$ single crystals for (a) $y = 6.35$ and (c) $y = 6.65$ at high (low) temperature shown by the thin (thick) lines.

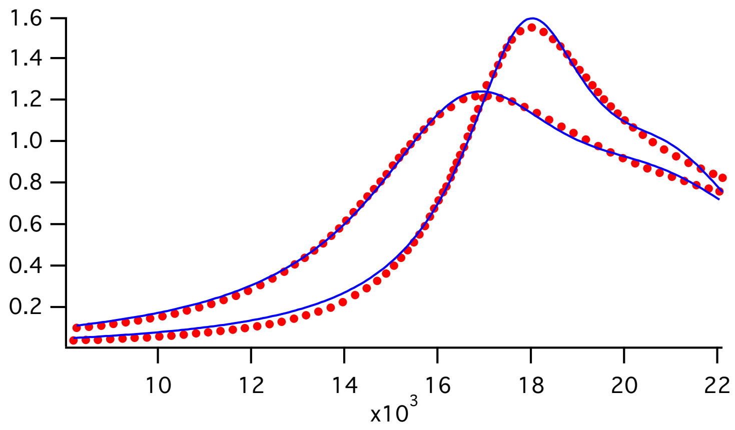

Figure 3.6: Imaginary part of the dielectric function $\epsilon_2(\omega)$ for temperature at 122 K and 447 K of La_2CuO_4 sample. The fit lines are obtained changing the parameters of two Lorentz oscillators as shown in details in the table.

of the band edge [Fan, 1951] given by:

$$E_g(T) = E_g^0 - 2\hbar\omega_0\alpha_p[n(\hbar\omega_0/k_B T) + 1] \tag{3.18}$$

where α_p is the polaron coupling constant. Moreover, including the coupling to a single phonon of frequency ω_0, the phonon scattering induces a decay rate of the quasiparticles and this gives:

$$\gamma(T) = 2^{3/2}\omega_0(\hbar\omega_0/E)^{1/2}\alpha_p[2n(\hbar\omega_0/k_B T) + 1] \tag{3.19}$$

where $E = \hbar\omega - E_g(T)$ denotes the total kinetic energy of the electron and hole. With this assumptions, increasing the temperature of the systems gives origin to a shift of the charge-transfer peak towards lower energies and also a broadening of the peak due to the coupling with the phonons. We have fitted the two curves at 122 K and 447 K with Lorentian oscillators and we have found that the predicted behaviour is correct as shown in Table 3.4. In order to fit correctly the experimental data, from 122 K to 447 K, is necessary to move the oscillator towards lower energies, broaden it but also increase its spectral weight.

	Oscillator Position (eV)	Oscillator Plasma Frequency (eV)	Oscillator Width (eV)
$T = 122$ K	2.23	1.10	0.41
$T = 447$ K	2.09	1.16	0.65

4 ARPES

The cuprate high-temperature superconductors have attracted great interest not only for the obvious application potential related to their high T_C , but also for their scientific significance. This systems highlight a major intellectual crisis in the quantum theory of solids, which, in the form of one-electron band theory, has been very successful in describing good metals (like Cu) but has proven inadequate for strongly correlated electron systems. In order to address the scope of the current approach in the quantum theory of solids and the validity of the proposed alternative models, a detailed comparison with those experiments that probe the electronic properties and the nature of the elementary excitations is required. In this context, angle-resolved photoemission spectroscopy (ARPES) plays a major role because it is the most direct method of studying the electronic structure of solids.

The energetics of the photoemission process and of the geometry of an ARPES experiment are sketched in Figure 4.1 and Figure 4. A beam of monochromatized radiation supplied either by a gas-discharge lamp or a synchrotron beamline is incident on a sample (which has to be a properly aligned single crystal, in order to perform momentum-resolved measurements). As a result, electrons are emitted by the photoelectric effect and escape into the vacuum in all directions. By collecting the photoelectrons with an electron energy analyzer characterized by a finite acceptance angle, one measures the kinetic energy $E_{kin}$of the photoelectrons for a given emission angle. This way, the photoelectron momentum $\mathbf{p}$ is also completely determined: its modulus is given by $p = \sqrt{2mE_{kin}}$ and its components parallel and perpendicular to the sample surface are obtained from the polar (θ) and azimuthal (ϕ) emission angles.

Within the noninteracting electron picture, and by taking advantage of total energy and momentum conservation laws (note that the photon momentum can be neglected at the low photon energies typically used in ARPES experiments), one can relate the kinetic energy and momentum of the photoelectron to the binding energy E_B

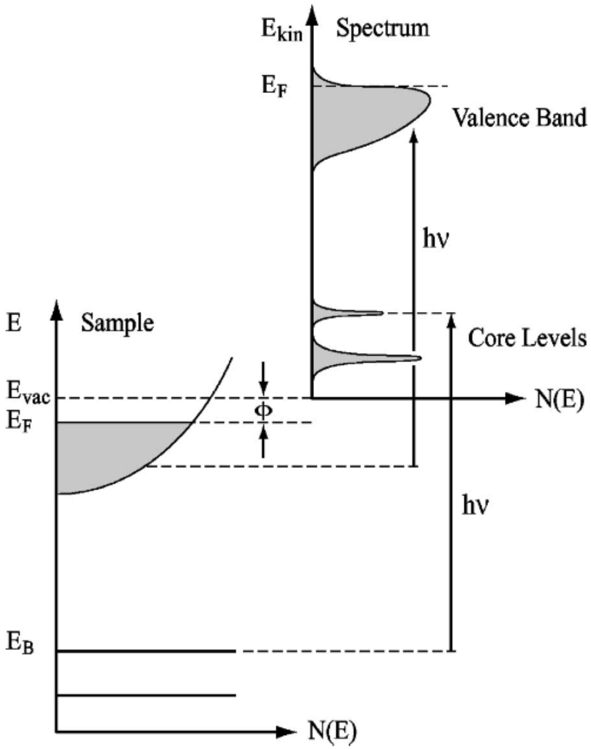

E_{kin}
Spectrum
E_F
Valence Band
hν
Core Levels
N(E)
E
Sample
E_{vac}
E_F
Φ
hν
E_B
N(E)

Figure 4.1: Energetics of the photoemission process. The electron energy distribution produced by incoming photons and measured as a function of the kinetic energy E_{kin} of the photoelectrons (right) is more conveniently expressed in terms of the binding energy E_B (left) when one refers to the density of states inside the solid ($E_B = 0$ at E_F). From [Hüfner, 1995]

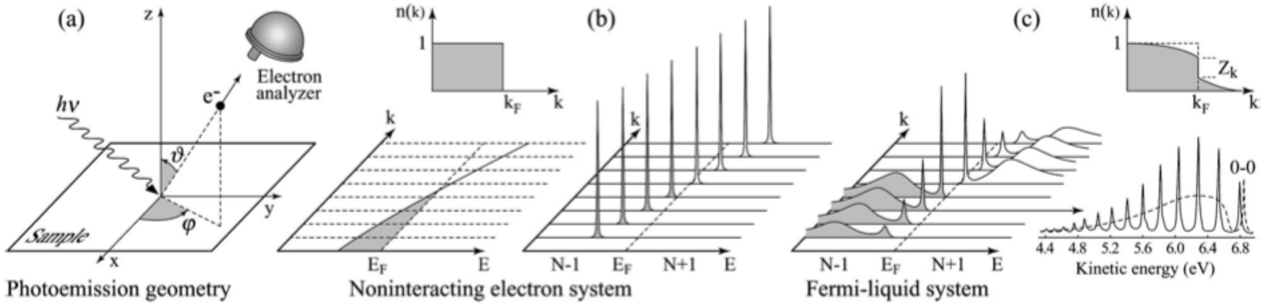

(a)
z
hν
e⁻
Electron analyzer
ϑ
φ
y
x
Sample
Photoemission geometry
n(k)
1
k_F
k
(b)
k
E_F
E
N-1
E_F
N+1
E
Noninteracting electron system
(c)
n(k)
1
Z_k
k_F
k
k
N-1
E_F
N+1
E
Fermi-liquid system
0-0
4.4
4.8
5.2
5.6
6.0
6.4
6.8
Kinetic energy (eV)

Figure 4.2: Angle-resolved photoemission spetroscopy: (a) geometry of an ARPES experiment in which the emission direction of the photoelectron is specified by the polar (θ) and azimuthal (ϕ) angles; (b) momentum-resolved one-electron removal and addition spectra for a noninteracting electron system with a single energy band dispersing across E_F; (c) the same spectra for an interacting Fermi-liquid system ([Sawatzky, 1989]). For both noninteracting and interacting systems the corresponding ground-state ($T = 0$K) momentum distribution function $n(\mathbf{k})$ is also shown. (c) Lower right, photoelectron spectrum of gaseous hydrogen and the ARPES spectrum of solid hydrogen developed from the gaseous one ([Sawatzky, 1989]).

and crystal momentum $\hbar\mathbf{k}$ inside the solid:

$$E_{kin} = h\nu - \phi - |E_B|; \tag{4.1}$$

$$\mathbf{p}_{\|} = \hbar\mathbf{k}_{\|} = \sqrt{2mE_{kin}} \cdot \sin\theta \tag{4.2}$$

Here $\hbar\mathbf{k}_{\|}$ is the component parallel to the surface of the electron crystal momentum in the extended zone scheme. Upon going to larger θ angles, one actually probes electrons with $\mathbf{k}$ lying in higher-order Brillouin zones. Note that the perpendicular component of the wave vector $\mathbf{k}_{\perp}$ is not conserved across the sample surface due to the lack of translational symmetry along the surface normal. This implies that, in general, even experiments performed for all $\mathbf{k}_{\|}$ (i.e., by collecting photoelectrons at all possible angles) will not allow a complete determination of the total crystal wave vector $\mathbf{k}$. A particular case in which the uncertainty in $\mathbf{k}_{\perp}$ is less relevant is that of the low-dimensional systems characterized by an anisotropic electronic structure and, in particular, a negligible dispersion along the z axis [i.e., along the surface normal; Figure 4(a)]. The electronic dispersion is then almost exclusively determined by $\mathbf{k}_{\|}$, as in the case of the 2D copper oxide superconductors. As a result, one can map out in detail the electronic dispersion relations $E(\mathbf{k}_{\|})$ simply by tracking, as a function of $\mathbf{p}_{\|}$, the energy position of the peaks detected in the ARPES spectra for different takeoff angles [as in Figure 4(b), where both direct and inverse photoemission spectra for a single band dispersing through the Fermi energy E_F are shown]. As an additional bonus of the lack of z dispersion, one can directly identify the width of the photoemission peaks with the lifetime of the photohole ([Smith et al., 1993]), which contains information on the intrinsic correlation effects of the system and is formally described by the imaginary part of the electron self-energy.

4.1 Three step model

To develop a formal description of the photoemission process, one has to calculate the transition probability w_{fi} for an optical excitation between the N-electron ground state Ψ_i^N and one of the possible final states Ψ_f^N. This can be approximated by Fermi's golden rule:

$$w_{fi} = \frac{2\pi}{\hbar}|\langle\Psi_f^N|H_{int}|\Psi_i^N\rangle|^2\delta(E_f^N - E_i^N - h\nu) \tag{4.3}$$

where $E_i^N = E_i^{N-1} - E_B^{\mathbf{k}}$ and $E_f^N = E_f^{N-1} + E_{kin}$ are the initial and final states energies of the N-particle system. The interaction with the photon is treated as a perturbation given by:

$$H_{int} = -\frac{e}{2mc}(\mathbf{A}\cdot\mathbf{p} + \mathbf{p}\cdot\mathbf{A}) = -\frac{e}{mc}\mathbf{A}\cdot\mathbf{p} \tag{4.4}$$

where **p** is the electronic momentum operator and **A** is the electromagnetic vector potential. At this point, a more rigorous approach is to proceed with the so-called *one-step model* in which photon absorption, electron removal, and electron detection are treated as a single coherent process. In this case bulk, surface, and vacuum have to be included in the Hamiltonian describing the crystal, which implies that not only bulk states have to be considered, but also surface and evanescent states, as well as surface resonances. However, due to the complexity of the one-step model, photoemission data are usually discussed within the *three-step model*, which, although purely phenomenological, has proven to be rather successful [Feibelman and Eastman, 1974]. Within this approach, the photoemission process is subdivided into three independent and sequential steps:

1. Optical excitation of the electron in the bulk.

2. Travel of the excited electron to the surface.

3. Escape of the photoelectron into vacuum.

The total photoemission intensity is then given by the product of three independent terms: the total probability for the optical transition, the scattering probability for the traveling electrons, and the transmission probability through the surface potential barrier. Step (1) contains all the information about the intrinsic electronic structure of the material. Step (2) can be described in terms of an effective mean free path, proportional to the probability that the excited electron will reach the surface without scattering (i.e., with no change in energy and momentum). The inelastic-scattering processes, which determine the surface sensitivity of photoemission, also give rise to a continuous background in the spectra which is usually ignored or subtracted. Step (3) is described by a transmission probability through the surface, which depends on the energy of the excited electron as well as the material work function ϕ.

In evaluating step (1), the problem simplifies within the *sudden approximation*, which is extensively used in many-body calculations of photoemission spectra from interacting electron systems and which is in principle applicable only to electrons with high kinetic energy. In this limit, the photoemission process is assumed to be sudden, with no post-collisional interaction between the photoelectron and the system left behind (in other words, an electron is instantaneously removed and the effective potential of the system changes discontinuously at that instant). The N-particle initial Ψ_i^N and final state Ψ_f^N can then be written as a product of single electron states $\phi_{i(f),\mathbf{k}}$ and the wavefunction of the remaining system $\psi_{i(f),\mathbf{k}}^{N-1}$:

$$\Psi_i = C\phi_{i,\mathbf{k}}\psi_{i,\mathbf{k}}^{N-1}, \qquad \Psi_f = C\phi_{f,\mathbf{k}}\psi_{f,\mathbf{k}}^{N-1} \tag{4.5}$$

where $\mathbf{k}$ denotes the wave vector of the photoelectron of energy E_{kin}. The factorization of the wave functions permits to write the intensity of the photocurrent in a simple form:

$$I(\mathbf{k}, \omega) = \sum_{i,f} w_{f,i} \propto |M(\mathbf{k}, \omega)|^2 A(\mathbf{k}, E) f(E) \tag{4.6}$$

where the single-electron matrix element $M(\mathbf{k}, \omega) \propto \langle \phi_{i,\mathbf{k}} | H_{int} | \phi_{f,\mathbf{k}} \rangle$ depends on the photon energy $\hbar\omega$ and the state $\mathbf{k}$ of the removed electron. The single-electron spectral function $A(\mathbf{k}E)$ describes the probability of removing an electron with energy E and momentum $\hbar\mathbf{k}$ from the system of N electrons. The Fermi function $f(E)$ takes into account that direct photoemission spectroscopy probes only the occupied electronic states. From the quantity $I(\mathbf{k}, \omega)$ it is possible to reconstruct a map of the population of the states in energy and momentum. This gives an immediate and detailed information on the band structure of the material. For a review see [Damascelli et al., 2003].

4.2 *Fermi Surface*

The low-energy electron excitations close to the Fermi surface (FS) determine many physical properties of metals and therefore the knowledge of the FS topology is very important for the characterization of the copper-oxide materials. Numerous investigations were devoted to studies of the shape and the doping dependence of the FS of cuprate superconductors. The experimental evidences confirms the existence of an FS in cuprate superconductors in agreement with theoretical band structure calculations. The recent improvement in the performance of ARPES measurements, and especially in getting high angle resolution which enables to provide high quality momentum distribution maps, were decisive in clarifying many controversial results of early experiments.

The most detailed studies of the excitation spectra near the Fermi surface have been performed for single crystals of $Bi_2Sr_2CaCu_2O_8$, which have a stable surface. The quasi-two dimensional nature of the electronic spectrum in Bi-based compounds, due to a weak dispersion along the k_z-direction, substantially simplifies the measurements of the photoemission spectra as a function of the in-plane momentum components. However, the study of the FS of the Bi2212 compounds is complicated by several secondary features besides those related to primary electronic structure. These are the diffraction replicas originating from the incommensurate modulation of the BiO layers, the shadow bands due to the superstructure formation, and the bilayer band splitting caused by the two CuO_2 planes in the Bi2212. The incommensurate modulation of the BiO layers can be suppressed using Pb-doped Bi2212 samples. A detailed and systematic ARPES investigation of the doping dependence of the normal-state FS of the Pb-Bi2212 crystals were performed by [Kordyuk et al., 2002] where six samples from the underdoped (UD, T_C = 76K) to the overdoped (OD, T_C = 69K) crystals were studied. Figure 4.3 shows the momentum distribution maps (MDM) for these two samples in (a) and (b) plots. The plot (c) is the same as (b) with the first Brillouin zone (BZ) shown by the white square and the main and the shadow Fermi surfaces emphasized by the black and white lines, respectively. The maxima of the MDM (the bright regions), which reflect the maxima of the MDCs measured at the Fermi energy, correspond to the FS. In addition to the main FS represented by the large hole-like rounded square or a "barrel" around (π, π) point in the BZ, the much weaker shadow bands shifted from the main FS by the wave vector (π, π) (the white arrows in the plot c) are also depicted. With increasing hole concentration x, the size of the FS barrels increases as can be seen in the decrease of the interbarrel separation at the $(\pi, 0)$ point in the (b) plot in comparison with the (a) plot. With doping, the FS shape changes from being quite rounded in the UD sample (a) to the form of a square with rounded corners in the OD sample (b) but no change in the FS topology was observed within the doping range studied. The FS shape changes in Figure 4.3 are accompanied by the intensity variation from the maximum values in the nodal directions$(0, 0) \rightarrow (\pi, \pi)$ at the FS barrel in the UD sample to a uniform distribution over the FS with faint maxima at antinodal $(\pi, 0)$ points in the OD sample. This reflects the variation of the density of electronic states (DOS) at different parts in the k-space of the FS with doping.

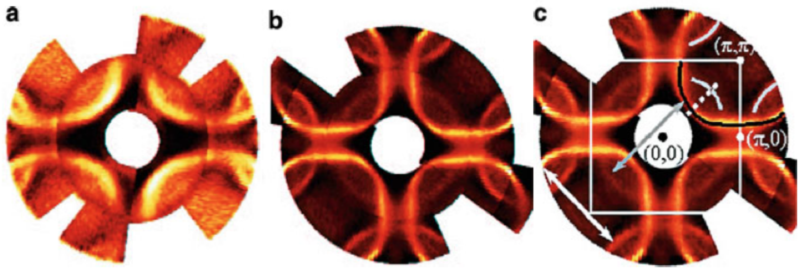

Figure 4.3: The normal-state (T = 300K) Fermi surface map of Bi$(\mathrm{Pb})-$2212: underdoped (UD, Tc = 76K) (a), overdoped (OD, Tc = 69K) (b). Panel (c) is the same as (b) with the first Brillouin zone shown by the white square and the main and the shadow Fermi surfaces emphasized by the black and white lines, respectively.

4.3 Metal-Insulator Transition

In early ARPES studies of lightly doped LSCO compounds, a ”two-component” electronic structure was observed in the ”antinodal” (AN) region close to the $(\pi, 0)$ point of BZ: a broad ”hump” at a large binding energy around -0.5 eV and a weak QP peak close to E_F which appears at $x \approx 0.05$. With doping, a weight transfer occurred from the broad hump to the QP peak at E_F, while in the nodal (N) direction, close to the $(\pi/2, \pi/2)$ point, the QP peak can be clearly resolved only at moderate doping $x \approx 0.15$ ([Damascelli et al., 2003]). This behavior was explained as reflecting the evolution of the in-gap states in the Mott insulator under doping with the chemical potential pinned inside the Mott gap as shown in Figure 4.5.

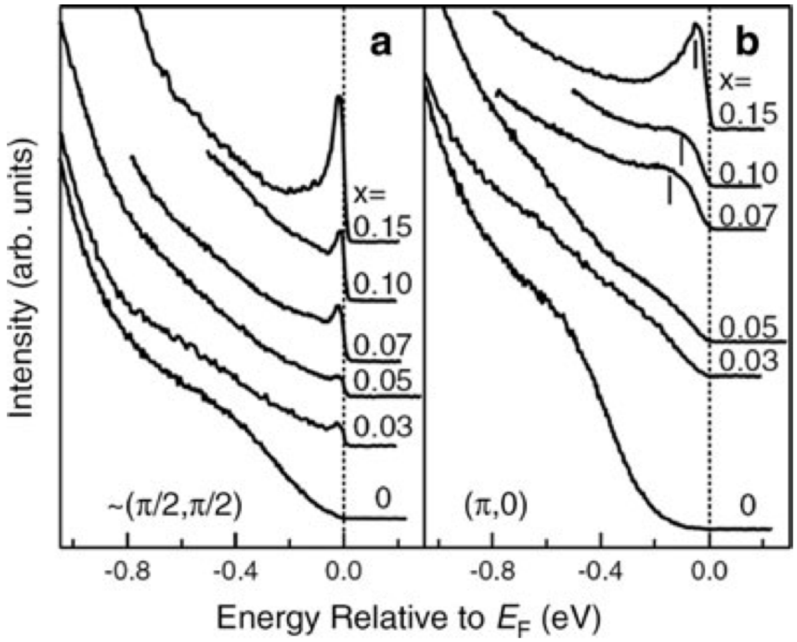

Figure 4.4: Energy distribution curves for $La_{2-x}Sr_xCuO_4$ at $\mathbf{k} = \mathbf{k}_F$ at various dopings: along the nodal direction $(\pi/2, \pi/2)$ (a) and at $(\pi, 0)$ (b).

Figure 4.4 shows the dependence with the doping of the EDCs for $La_{2-x}Sr_xCuO_4$ at $\mathbf{k} = \mathbf{k}_F$ in the vicinity of the N point $(\pi/2, \pi/2)$ (a) and at the AN point $(\pi, 0)$ (b) of the BZ. The QP peak in the N direction is already visible at $x = 0.03$ and its intensity increases with the doping. In contrast, the AN EDCs show pseudogap behavior for the doping region $x \leqslant 0.15$.

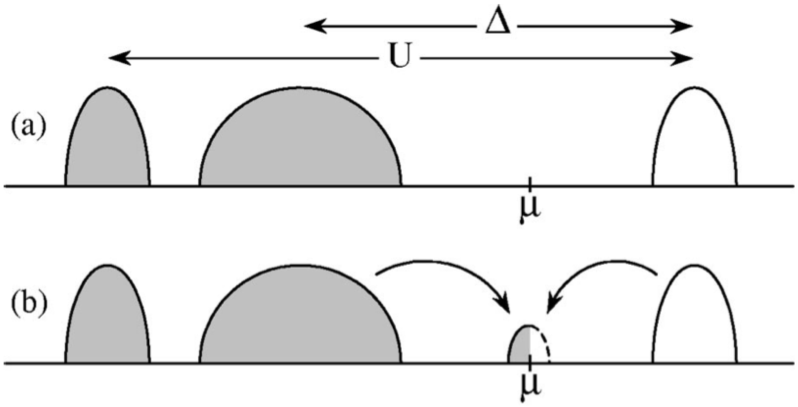

Figure 4.5: Doping of a charge-transfer insulator: (a) in the undoped insulator a gap Δ separates the occupied from the unoccupied electronic states; (b) upon doping, μ is pinned inside the charge-transfer gap and states move towards the chemical potential. [van Veenendaal and Sawatzky, 1994]

4.4 Laser ARPES

To investigate the valence (occupied) electronic states in the solids, various incoming photon energies in photoionization are used. The photon energy in the ultraviolet regime ($E_i = 5 - 100\text{eV}$) (ultraviolet photoemission spectroscopy - UPS) is used to study low energy electronic states close to the Fermi energy in metals. High energy (few mega electron volt) and momentum resolutions achieved in recent years at photoemission beamlines on high-flux synchrotron facilities enables one to obtain electron dispersion curves in metals with high precision in ARPES (for a review, see [Damascelli et al., 2003]). In the X-ray regime ($E_i > 1000\text{eV}$) (X-ray photoemission spectroscopy - XPS), one can study only electron density of states due to the low momentum resolution. Recently, a new low-photon regime around 6eV was accessed with the help of laser-based ARPES [Koralek et al., 2006]. Studies of $Bi_2Sr_2CaCu_2O_{8+\delta}$ crystals with the new technique demonstrated a much better resolution and a low background (see Figure 4.6). The low-energy laser ARPES is significantly more bulk sensitive since the electron mean free paths at this energy increase up to 16 Å in comparison with $\sim$ 6 Å in standard ARPES studies with 52 eV photons (see Figure 4.7).

4.5 Laser ARPES setup

In order to develop novel skills in the field of state-of-the-art electron spectroscopies, I spent one year at the University of British Columbia working in the ARPES laboratory led by prof. Andrea Damascelli. Here, I learned how to manage an ARPES experiment and I had the opportunity to build an optical setup from scratch, wich has been coupled to the conventional ARPES in order to obtain time-

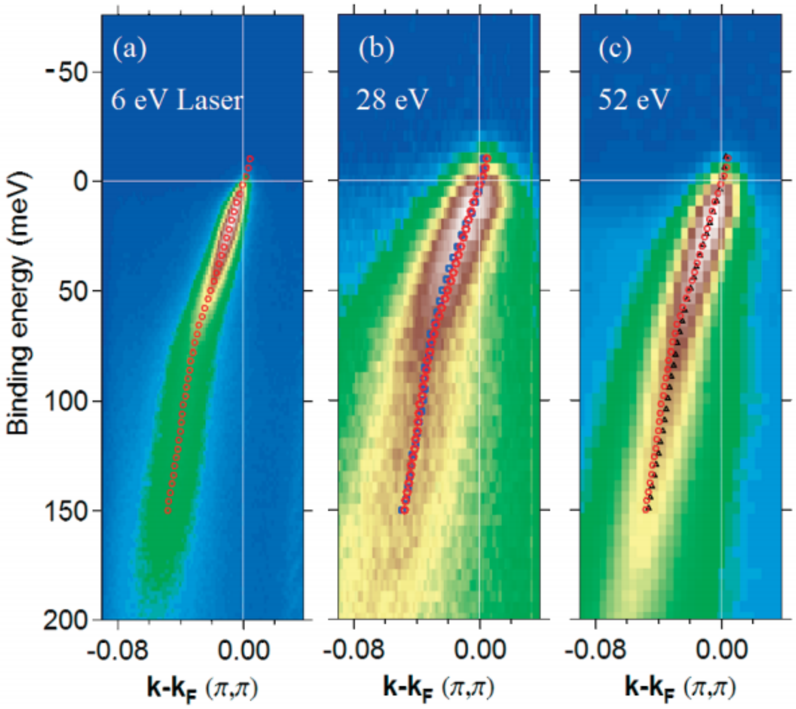

Figure 4.6: Comparison of ARPES along the node in near optimally doped Bi2212 using (a) 6 eV laser photons at $T = 25$KT, (b) 28 eV photons at $T = 26$K, and (c) 52 eV photons at $T = 16$K. The images are scaled identically in E and $\mathbf{k}$, and all three contain MDC derived dispersion for the laser data (red circles). Additionally, the dispersions for the data of panels (b) and (c) are shown as blue squares and black triangles, respectively. From [Koralek et al., 2006]

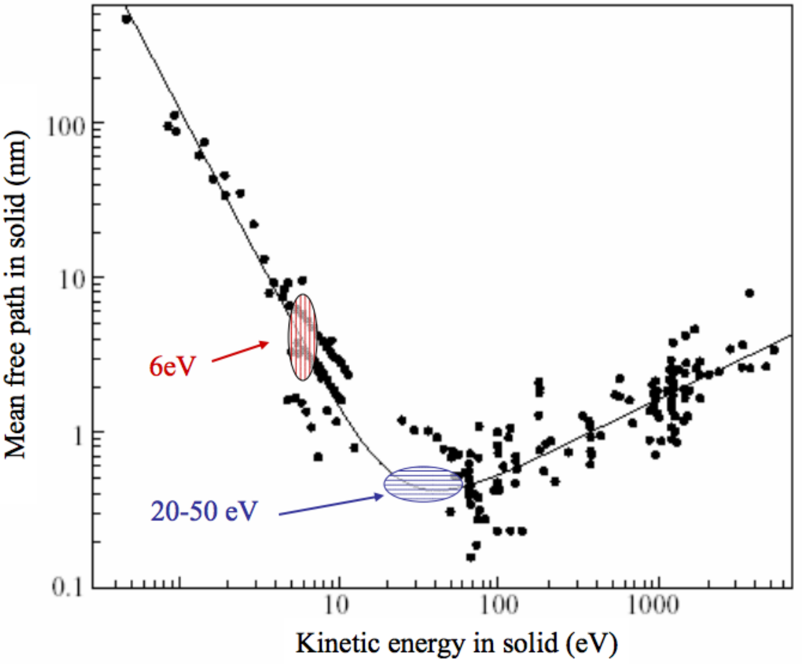

Figure 4.7: The "universal curve" for surface sensitivity in photoemission. Electron inelastic mean free paths from a variety of materials are plotted versus kinetic energy relative to E_F (the lowest kinetic energies shown will not be able to overcome the work function). Indicated on the plot are the kinetic energy ranges for standard ARPES and laser ARPES. From [Seah and Dench, 1979]

resolved photoemission. After having achieved the best configuration to optimize the time- energy-resolution, I focused my attention on different classes of materials: I studied the static photoemission spectrum of the Bi2201 copper oxide, looking at the difference in its Fermi surface using different photon energy (1.5 eV, 3 eV, 6 eV).

We illustrate our setup for Time- and Angle-Resolved Photoemission Spectroscopy (tr-ARPES) in Figure 4.8. A Ti:Sapphire oscillator generates 820 nm infrared (IR) laser pulses, which are split into two paths with a tunable intensity ratio using a polarizing beamsplitter. In the probe path, two second harmonic generation stages in series produce the 205 nm ultraviolet (UV) beam. In the pump path, a delay stage varies the optical path length to control the pump-probe delay with 10 fs precision. The IR has a spectral Full-Width-Half-Maximum (FWHM) of ~ 21 nm. Once the 205 nm beam has been produced the pump and the probe beam are driven into the chamber and focalized on the sample. In order to characterize this system we performed some measurements on a gold sample and we found that the overall energy resolution (combining the resolution of the analyzer with the resolution of the laser light) is $\simeq 10$ meV.

I studied the effect of the polarization of the laser light in the photoemission spectrum of the Na2IrO3 Iridate; I performed low energy photoemission on the Bi2Se3 topological insulator and I started an experiment aimed at tracking the dynamics of the quasi-particle peak around the nodal region of the Fermi Surface of Bi2212 cuprate. Concerning the present work, we want to present a measurement on the $Bi_2Sr_{2-x}La_xCuO_{6+\delta}$ OP16 sample using the laser-ARPES system to show the Fermi surface of such a sample and comparing it with data already presented in literature to validate our results.

4.6 Laser ARPES measurements on Bi2212

In the BCS theory of conventional superconductors, the superconducting phase transition is accompanied by a modification of the electronic density of states over a frequency range of the order of the superconducting gap (SC), without significantly affecting the physical properties at higher energies. In contrast to this, in strongly correlated systems like cuprates, the electronic properties at the Fermi energy (E_F) are intertwined with those at high-energy scales. One of the pivotal challenges in the field of high-temperature superconductivity is to understand whether and how the high-energy scale physics associated to high-energy Mott-like excitations ($|E - E_F| > 1$ eV) is involved in the condensate formation. A huge effort is currently devoted to develop novel spectroscopic techniques, beyond conventional spectroscopies at equilibrium, to provide new informa-

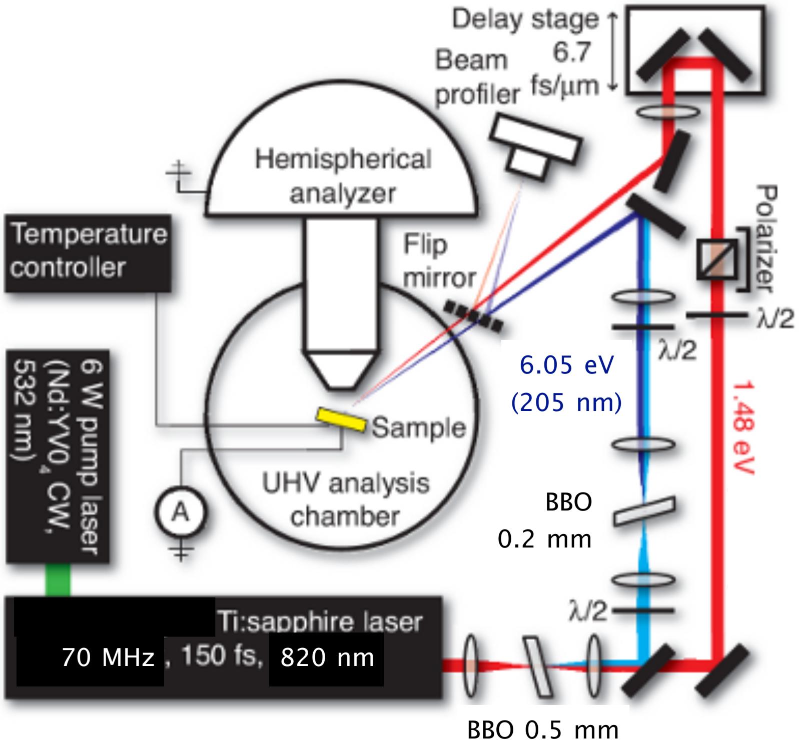
Delay stage
6.7 fs/µm
Beam profiler
Hemispherical analyzer
Temperature controller
Flip mirror
Polarizer
λ/2
λ/2
6.05 eV (205 nm)
1.48 eV
6 W pump laser (Nd:YVO$_4$, CW, 532 nm)
Sample
UHV analysis chamber
A
BBO 0.2 mm
λ/2
Ti:sapphire laser
70 MHz, 150 fs, 820 nm
BBO 0.5 mm

Figure 4.8: Laser-ARPES setup based on the generation of the fourth harmonic (6 eV) of a Ti:Sapphire output. The path of the residual IR beam is controlled by a delay stage to perform pump-probe experiments. Once the 205 nm beam has been produced the pump and the probe beam are driven into the chamber and focalized on the sample to do time-resolved ARPES.

tions and solve this issue, paving the way to finally develop a theory to explain high temperature superconductivity.

Following this approach, with the laser-ARPES system that I have developed, after first characterizations, we have measured the Fermi surface of the double-layer copper oxyde Bi2212 at T=8 K. This system will be treated in detail in Chapter 7. In Figure 4.9 we report the first measurement of the Bi2212 Fermi surface obtained with the laser-ARPES setup at UBC Vancouver. In the drawing on the right, the investigated part of the Brillouin zone for the measurement is highlighted in red. From this measurement it is possible to see that the bonding band (BB) and antibonding band (AB) of the CuO_2 bilayer are clearly resolved in the momentum space. The two concentric arcs that are visible around the gamma point are due to the well known replica of the Brillouin zone in this compound ([Kordyuk et al., 2002]).

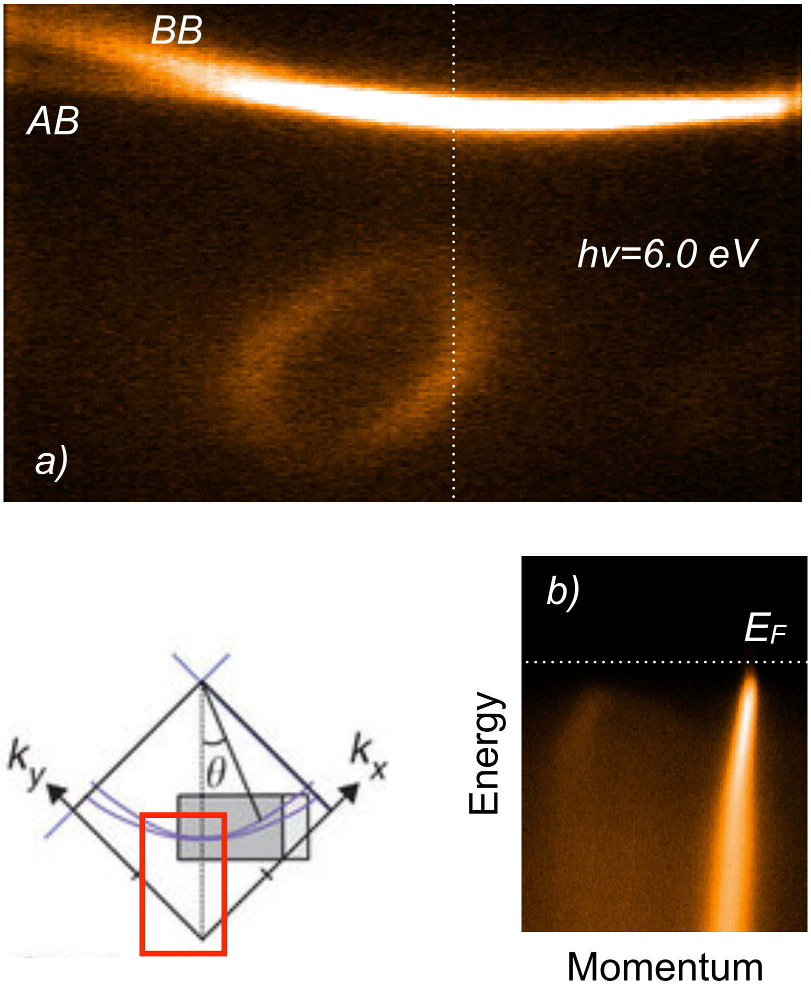

Figure 4.9: a) Bi2212 fermi surface measured with the laser-ARPES setup of the ARPES Laboratory at the University of British Columbia in Vancouver. The red highlighted part of the Brillouin zone can help to read the measurements. The bright signal refers to the typical momentum-space mappings of this compound. the bonding band (BB) and antibonding band (AB) of the CuO_2 bilayer are visible. The two concentric arcs that are visible around the gamma point are due to the well known replica of the Brillouin zone in this compound. b) Energy versus momentum plots of the spectral image along the Fermi surfaces identified by dotted white line in panel a.

In order to validate our first measurements we have compared them with similar measurements already present in literature. In Figure 4.10 we have reported the Fermi surface of the same sample measured by [Anzai et al., 2013]. The comparison between the two measurements in Figure 4.9 and Figure 4.10 is good.

In respect to the original plan, the system cannot performe yet time-resolved measurements. This is due to the high repetition rate (70 MHz) of the oscillator having enough average power to thermally destroy the superconductivity of the system even at very low temperature. This results in an impossibility to follow the weak change of the bands structure driven by the pump. Nowadays improvements on this system are in progress. The idea is to change the laser source switching to a low rep-rate amplified system that reduces the average power of the pump and, at the same time, increases its energy per pulse.

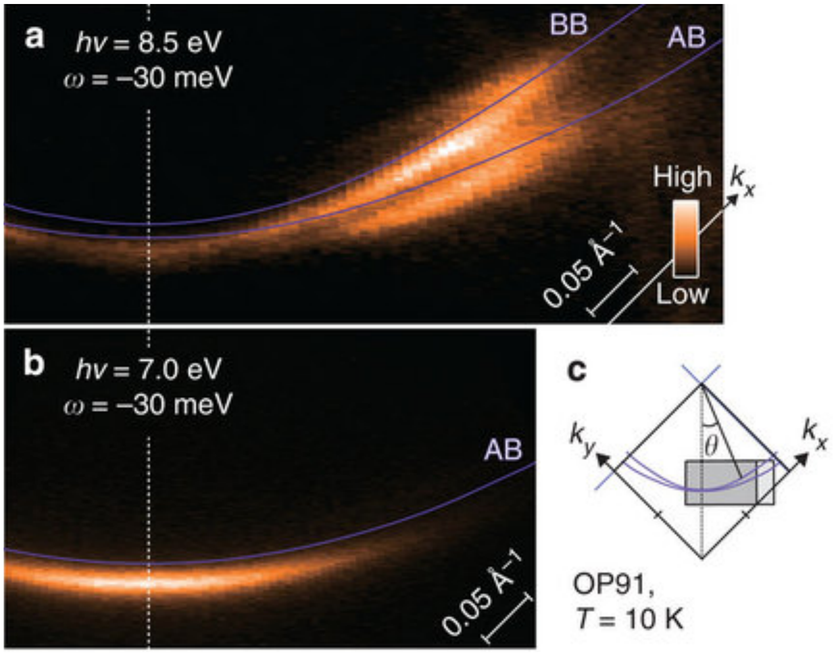

Figure 4.10: APRES data taken with different low-energy photons. The data were collected at T=10 K for an optimally doped Bi2212 with Tc=91 K (OP91). (a,b) Momentum-space mappings at the Fermi level, taken with $h\nu = 8.5$ and 7.0 eV, respectively, over the fields of view marked by grey rectangles in c. The globally resolved doublet is ascribed to the BB (bonding band) and AB (antibonding band) of the CuO_2 bilayer. Purple curves denote the Fermi surfaces. (c) Schematic of a Brillouin-zone quadrant. [Anzai et al., 2013]

5 Experimental Systems

5.1 Optical Oscillator

The first stage of the laser system is a diode pumped Nd:Yag laser (Coherent Verdi V10) which provides a beam with wavelenght $\lambda = 532$ nm and maximum output power of 10 W. This laser pumps a Ti:sapphire oscillator (Coherent Mira 900) converting the input continuous wave beam into a train of ultrafast pulses characterized by a wavelenght $\lambda = 800$ nm and a temporal width of 120 fs. The cavity of the oscillator is equipped by a cavity dumper which is an acousto-optical switch that allows to vary continuously the repetition rate of the laser from 1 MHz to 200 Hz and to increase the energy per pulse. The output energy per pulse is about 50 nJ at 100 KHz of repetition rate. This experimental configuration is particularly suitable to study the strong non-equilibrium regime in cuprates avoiding the avarage heating effects. At the output of the laser source, a telescope formed by two plano-convex lenses (L) placed at the distance 2f from each other (f is the focus length of the lens) collimates the beam and helps in obtaining a better focalization on the sample at the end of the line. The beam is divided in two part by a beam splitter (BS): the 70 % of the incident beam is trasmitted (pump) while the remaining 30 % is used as probe. The temporal delay between the two beam is varied by a motorized high-precision translational stage, placed on the pump line, which is controlled via software and allows to change the optical path in step of 1 μm. Because of the double passage into the translational stage 1 μm corresponds to a temporal delay between pump and probe of 6.6 fs. The intensity of both the beams is tuned by an intensity attenuator given by an half-wave plate and a polarizer (P). Pump and probe are both focused on the sample with a plano-convex lens of 20 cm and 10 cm and have perpendicular polarizations to avoid any possible interference effect. A mirror placed on a piezoelectric motor allows to obtain a fine control of the spatial coincidence. Since the relative variations of the probe are very low (tipically of the order of 10-5 is necessary to minimize all the effects due to scattering of the pump. The size of the two beams are measured by imaging the spots in the focal plane on a CCD camera. The samples measured are placed in an closed-cycle cryostat that can cool down to the minimum temperature of 10K (Nevertheless, all the measurements done on this system are at room temperature).

Supercontiuum light is produced on the probe line, focusing the probe pulses with an aspherical lens into a photonic crystal fiber. The fiber is positioned on a home-made launch system equipped by three traslational degrees of freedom and a tilting mechanism, in order to optimize the coupling of the laser into the fiber itself. Strongly non linear processes inside the fiber broaden the 800 nm pulse generating a broadband pulse characterized by a spectral content ranging from 450 nm to 1500 nm and a complex spectral chirp. More details on the temporal and spectral characterization of the supercontinuum light will be given in the next chapter. After the fiber the white light pulse is parallelized by an achromatic doublet (AD) and then refocused by another doublet with focal lenght f=100 mm. An optical window, placed before the last doublet, samples the probe. This reference is used to monitor and compensate the probe intensity during the measurements. Both the reference and the signal reflected by the sample are dispersed by a prism and collected by two Si-arrays of 128 pixels. A spectral slice, whose width ranges from 2 nm at 700 nm to 6 nm at 1100 nm, is acquired by each pixel of the array, corresponding to a constant temporal resolution of $\sim$120 fs [Cilento et al., 2010]. A fast digitizer performs the scan of the arrays. Because of the large difference between the scan frequency of the array and the repetition rate of the laser, a single-shot detection is not feasible and it is necessary to integrate many pulses. The pump beam is chopped at a low frequency (typically 30 Hz), and, at the same time, the pump modulation is acquired by a photodiode and digitalized by a data acquisition device (NI-DAQmx M-series) which is synchronized with

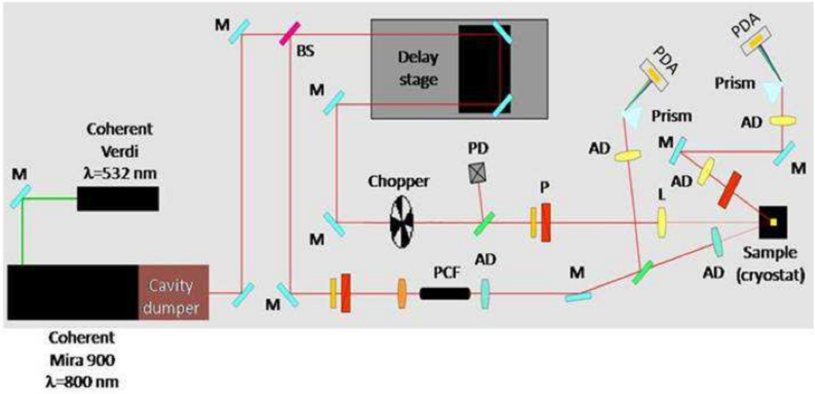

Figure 5.1: Schematic drawing of the experimental setup, located at Universita' Cattolica in Brescia, to perform time-resolved spectroscopic measurements. Key elements are the Photonic Crystal Fiber employed to generate the supercontinuum pulse, and the acquisition system based on fast linear array sensors.

the fast digitizer. In this way it is possible to discriminate between pumped and the unpumped pulses. At the end of a single acquisition the pump-induced variation of signal is obtained by mediating and subtracting the two signals. To prevent the probe intensity fluctuations from affecting the measurement, the reflectivity variation is divided by the reference signal. The sensitivity of the array of photodiodes ranges from 500 nm to about 1000 nm, outside this range the response of the photodiodes drops. Only this portion of the supercontinuum light will be used in the measurements reported in this work.

5.2 *Optical Parametric Amplifier*

Nowadays, mainstream ultrashort pulse generation technology is based on Ti:sapphire lasers with Kerr-lens mode-locking and chirped-pulse amplification (CPA) [Backus, 1998], which provide highly stable and energetic pulses. However, the frequency tunability of such laser sources is limited in a narrow range around the fundamental frequency (FF) of 0.8 μm or around its second harmonic (SH) of 0.4 μm. Despite this limitation, the very high peak power of these sources enables exploiting the second-order nonlinear optical effect known as optical parametric amplification (OPA) [Boyd, 2003] [Shen, 2003] [Baumgartner and Byer, 1979] [Giordmaine and Miller, 1965] to extend their tuning range. The principle of OPA is quite simple

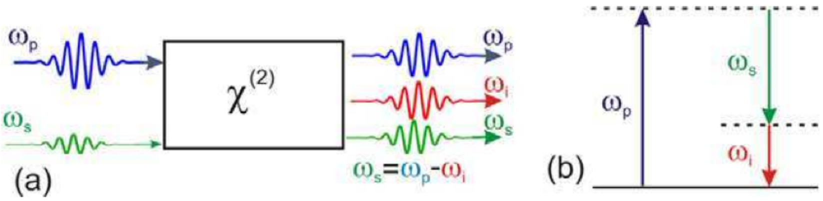

Figure 5.2: (a) Principle scheme of the OPA process; (b) photon energy balance in the OPA process.

(Figure 5.2): in a suitable nonlinear crystal, energy is transferred from an high frequency and high intensity beam (the pump beam, at frequency ω_P) to a lower frequency, lower intensity beam (the signal beam, at frequency ω_S), which is thus amplified. In addition a third beam (the idler beam, at frequency ω_i) is generated. The OPA process can be given a simple corpuscular interpretation (Figure 5.2): a photon at frequency ω_P is absorbed by a virtual level of the material and a photon at frequency ω_S stimulates the emission of two photons, at frequencies ω_S and ω_i, respectively. In this interaction both energy conservation

$$\hbar\omega_P = \hbar\omega_S + \hbar\omega_i \tag{5.1}$$

and momentum conservation

$$\hbar k_P = \hbar k_S + \hbar k_i \tag{5.2}$$

should be fulfilled. This last condition is also known as 'phase matching' and is the key requirement that needs to be satisfied to allow for efficient energy transfer between pump and signal/idler beams. The signal frequency to be amplified can vary in principle from $\omega_P/2$ (the so-called degeneracy condition, with $\omega_S = \omega_i$) to ω_P, and correspondingly the idler varies from $\omega_P/2$ to 0 (as a matter of fact the lowest frequency is limited by absorption of the nonlinear crystal). In summary, the OPA process transfers energy from a high-power, fixed-frequency pump beam to a low-power, variable-frequency signal beam, generating an idler beam to satisfy energy conservation. The OPA process thus provides an optical amplifier with continuously variable center frequency and represents an easy way of tuning over a broad range the frequency of an otherwise fixed femtosecond laser system. On the other hand, if suitably designed, an OPA can satisfy the phase matching condition over a very broad frequency range and can thus efficiently transfer energy from a narrowband pump pulse to a broadband signal pulse; it thus becomes a broadband amplifier which can be used to dramatically shorten, by more than an order of magnitude, the duration of the pump pulse. One can therefore start with a femtosecond system producing relatively long pulses (100-200 fs) and use an OPA to shorten their duration to the sub-10 fs regime. Figure 5.3 shows the conceptual architecture of a broadband OPA [Cerullo, 2003]. The system is powered by energetic femtosecond pulses, typically produced by an amplified Ti:sapphire laser at 800 nm. A fraction of the beam is split and used to produce the broadband seed beam by white light continuum (WLC) generation in a sapphire plate [Reed et al., 1994]. Then the pump beam (which may be optionally frequency-doubled) and the seed, after their timing has been adjusted by a delay line, interact in a first amplification stage. It is possible to further amplify the signal in a second stage (power amplifier), using a previously split fraction of the pump beam. Finally, a pulse compressor is used to correct the spectral phase distortions of the amplified beam and achieve nearly transform-limited (TL) pulse duration.

Let us first calculate the phase matching bandwidth of an OPA. In the limit of monochromatic plane waves and neglecting pump beam depletion, the gain of an OPA crystal with length L can be written as

$$G = \frac{I_{out}}{I_{in}} = 1 + \left[\frac{\Gamma}{g}\sinh(gL)\right]^2 \tag{5.3}$$

where $g = \sqrt{\Gamma^2 - (\frac{\Delta k}{2}))^2}$ is the small gain, $\Delta k = k_p - k_s - k_i$ is the

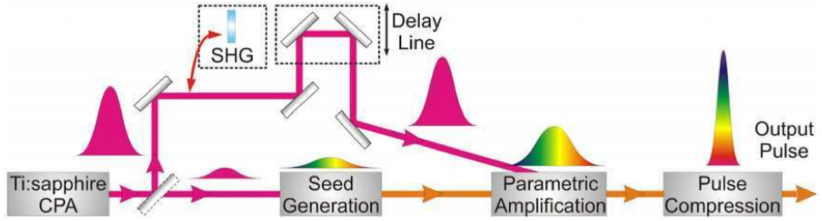

Figure 5.3: Conceptual scheme for a broadband OPA.

so called wavevector mismatch, $\Gamma^2 = \frac{2d_{eff}^2\omega_i\omega_s}{c_0^3\epsilon_0 n_i n_s n_p} I_p$, I_p is the pump intensity and d_{eff} is the effective nonlinear optical coefficient. Ideally one would like to have a broadband amplifier, i.e. an amplifier which, for a fixed pump frequency ω_p, provides a more or less constant gain over a broad range of signal frequencies. In order to achieve broadband amplification, one needs to keep the phase mismatch Δk as small as possible over a large bandwidth. Practically, however, the phase matching condition can be satisfied only for a given set of frequencies $(\tilde{\omega_i}, \tilde{\omega_p}, \tilde{\omega_s})$, so that

$$\Delta k = k(\tilde{\omega_p}) - k(\tilde{\omega_s}) - k(\tilde{\omega_i}) \tag{5.4}$$

As well explained in details in [Cirmi et al., 2007], the wavevector mismatch can be approximated to first order as

$$\Delta k \cong \delta_{si}\Delta\omega \tag{5.5}$$

where $\delta_{si} = \frac{1}{v_{gi}} - \frac{1}{v_{gs}}$ is the group velocity mismatch (GVM) between signal and idler pulses. The full width at half-maximum (FWHM) parametric gain bandwidth can then be calculated from equation 5.3 as

$$\Delta\nu = \frac{2(\log 2)^{1/2}}{\pi}\left(\frac{\Gamma}{L}\right)\frac{1}{|\delta_{si}|} \tag{5.6}$$

This equation makes it clear that, in order to obtain broad phase matching bandwidths, one must achieve, for a given signal frequency $\tilde{\omega_s}$, the group velocity matching between signal and idler pulsese, i.e. $\delta_{si} = 0$. It will then become possible to amplify a broad bandwidth centered around $\tilde{\omega_s}$. By using suitable nonlinear crystals, pump frequencies and phase matching configurations, $\tilde{\omega_s}$ can be varied over a very broad range, spanning from the ultraviolet to the mid-infrared. This enables the generation of widely tunable few-optical-cycle light pulses from OPAs. Figure 5.4 shows the gain bandwidths, as calculated using equation 5.3, of collinear degenerate OPAs pumped by the SH, panel (a), and the FF of Ti:sapphire, panel (b). In both cases a type I configuration and β-barium borate (BBO) crystal are considered, with 1 and 3 mm thickness, respectively. It can be seen that the gain bandwidth can be further broadened by slightly detuning from the optimum condition. In this way, phase matching is achieved simultaneously at two wavelengths to the blue and to the red of the degeneracy point, obtaining a two-peaked spectrum with broader bandwidth. The spectrum of the FF-pumped OPA has an FWHM of about 90 THz corresponding to a TL pulsewidth of 8.2 fs (1.6 cycles of the 1600 nm carrier wavelength) while that of the SH-pumped OPA is 100 THz, corresponding to 6.5 fs TL pulses (2.4 cycles of the 800 nm carrier). The near-IR OPA is thus able to generate bandwidths that are a larger fraction of the If the signal wavelength is tuned

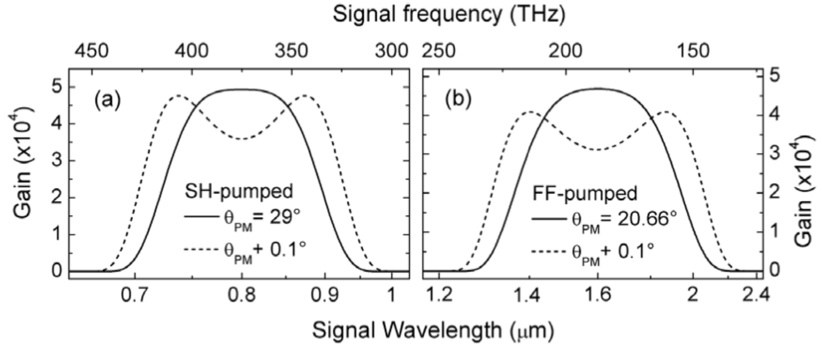

Figure 5.4: Calculated gain bandwidths for SH-pumped (a) and FF-pumped (b) degenerate OPAs using 1 mm thick and 3 mm thick BBO crystals, respectively.

away from degeneracy condition $\omega_S = \omega_i$, then the δ_{si} condition is generally lost in a collinear configuration, leading to narrow phase matching bandwidths. An additional degree of freedom can be introduced using a non-collinear geometry [Gale et al., 1995] [Gale et al., 1998], such as that shown in figure Figure 5.5(a). In this case, pump and signal wavevectors form an angle α (independent of signal wavelength) and the idler is emitted at an angle Ω with respect to the signal. In such a way, for a collinear geometry (Figure 5.5(b)), signal and idler moving with different group velocities get quickly separated, giving rise to pulse lengthening and bandwidth reduction, while in the non-collinear case (Figure 5.5(c)) the two pulses manage to stay effectively overlapped. The concept of non-collinear phase matching, as applied to an OPA, gives rise to the so-called non-collinear OPA (NOPA) scheme. In particular the visible NOPA [Tzankov et al., 2006] [Cerullo et al., 1998], pumped at 400 nm by the SH of Ti:sapphire and using a type I BBO crystal, is a very popular source. Using BBO, the NOPA concept works well in different wavelength regions such as in the blue-green spectral range, when pumped by the third harmonic of Ti:sapphire [Tzankov et al., 2002]. As an example, Figure 5.6(a) shows the calculated gain bandwidth for a 400 nm pumped visible NOPA, which extends from 500 to 750 nm while Figure 5.6(b) shows the calculated gain bandwidth of the

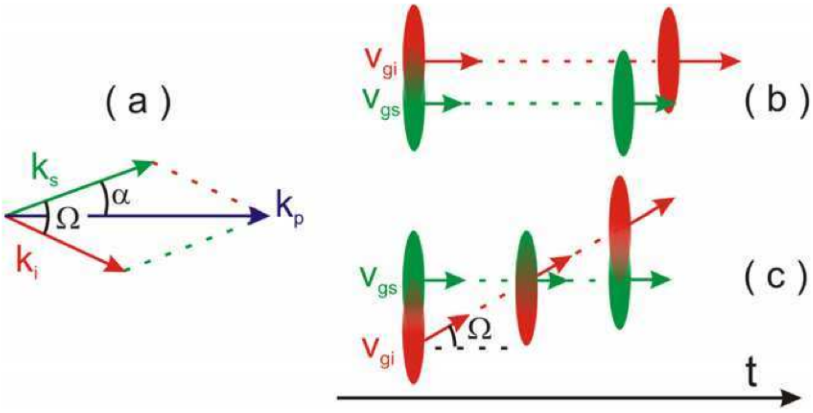

Figure 5.5: (a) Schematic of a non-collinear interaction geometry; (b) representation of signal and idler pulses in the case of collinear interaction; and (c) same as (b) for non-collinear interaction.

FF-pumped near-IR NOPA using a PPSLT crystal: it extends over 90 THz and corresponds to a TL pulsewidth of about 8 fs (1.8 cycles of the 1350 nm carrier wavelength). A typical visible NOPA design [Manzoni et al., 2006]is shown in a schematic picture in Figure 5.7 The system starts with a conventional CPA Ti:sapphire laser generating 150 fs, 800 nm pulses at 1 kHz with energy up to 500 μJ. The energy is sufficient for simultaneously pumping several independent NOPAs. A fraction of the beam is used to generate the 400 nm pump pulses, with energy up to 30 μJ, by SHG in a 1 mm thick BBO crystal. Another small fraction of the beam, with energy of approximately 2 μJ, is focused into a 1 mm thick sapphire plate to generate a highly stable single-filament white-light-continuum (WLC) seed. The chirp of the visible portion of the WLC is small and fairly linear with frequency. To avoid the introduction of additional chirp, only reflective optics are employed to guide the white light to the amplification stage. Parametric gain is achieved in a 1 mm thick BBO crystal, cut for type I phase matching ($\theta = 32\circ$, $\phi = 0\circ$),

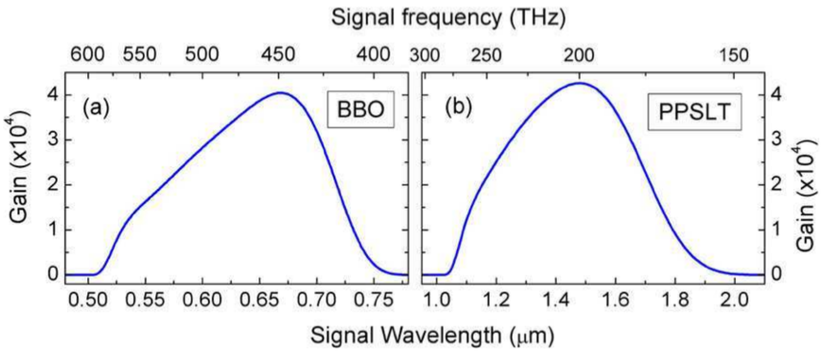

Figure 5.6: Calculated gain bandwidths for an SH-pumped NOPA in BBO (a) and an FF-pumped NOPA in PPSLT.

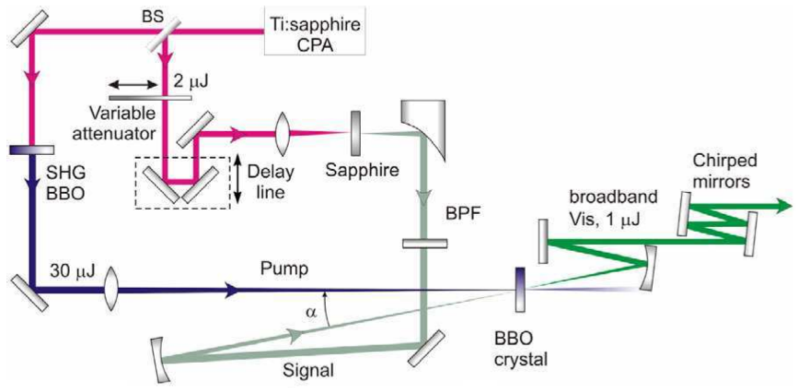

Figure 5.7: Scheme of a BBO based NOPA pumped at 400 nm. BS: beam-splitter; SPF: short-pass filter.

using a single-pass configuration to increase the gain bandwidth. The chosen crystal length is close to the pulse splitting length for signal and pump in the visible wavelength range. To minimize the effects of self-focusing, we place the BBO crystal beyond the focus of the pump beam. In that position the pump spot size is approximately 120 μm, corresponding to an intensity of 120 GW cm^{-2}; at higher intensities distortions and beam break-up are observed. The WLC seed is imaged by a spherical mirror in the BBO crystal, with a 100 μm spot size matching that of the pump beam. A 1 mm thick short-pass filter removes the strong residual FF component from the WLC, preventing its parasitic amplification. When the BBO crystal is illuminated by the pump pulse and aligned perpendicularly to the pump beam, it emits a strong off-axis parametric superfluorescence in the visible in the form of a cone with an apex angle of $\sim 6.2\circ$ (corresponding to an angle of $3.82\circ$ inside the crystal). This is the direction for which the group velocities of signal and idler are matched and therefore the gain bandwidth is maximized. The visible cone gives a visual aid to the identification of the optimum condition for broadband generation, which is achieved when the pump-signal angle matches the cone apex angle. In this condition, for optimum pump-seed delay, an ultra-broad gain bandwidth that extends over most of the visible is observed. A typical amplified pulse spectrum, shown in Figure 5.8(a), displays a bandwidth of 180 THz. The amplified pulses from a single stage have an energy of approximately 2 μJ, peak-to-peak fluctuations lower than 2% and good TEM_{00} beam quality. Much higher energies, up to ~ 300 μJ [Tzankov et al., 2006], can be extracted by a second amplification stage. After the gain stage the amplified pulses are collimated by a spherical mirror and sent to the compressor. Several compressor schemes have been implemented for the visible NOPA. Simple prism pairs can correct the GDD but not third-order

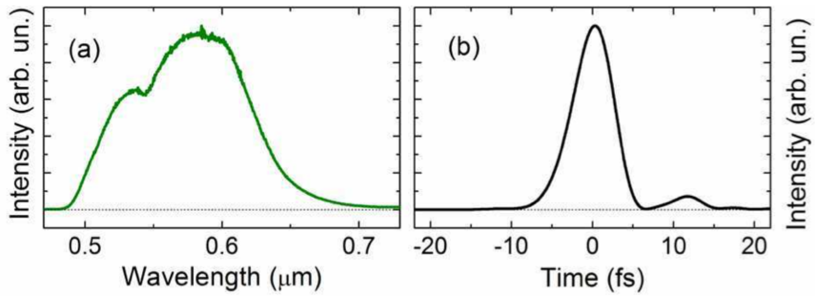

Figure 5.8: (a) Spectrum of the SH-pumped visible NOPA; (b) retrieved temporal intensity profile following compression by chirped mirrors, as measured by SPIDER.

dispersion and thus can only compress the pulses down to 10-15 fs. Sub-10 fs pulses can be achieved by using either prism-grating [Shirakawa et al., 1998] or prism-chirped mirror combinations, as well as adaptive compressors based on deformable mirrors [Baltuška et al., 2002]. We chose to use a compressor employing exclusively chirped mirrors [Cerullo et al., 1999]; this approach, besides the high energy throughput and the broadband phase correction, greatly simplifies the system design, allowing for compactness, insensitivity to misalignment and high day-to-day reproducibility, which are of great importance in practical applications. The resulting pulse length, as shown in Figure 5.8(b) is 5.7 fs that is close to the TL value and corresponds to less than three cycles of the carrier wavelength.

5.3 XUV-Laser Photoemission

Time-resolved measurements on Bi2212 shown in the Chapter 7 of the present work have been performed on the ARTEMIS beam line at the Central Laser Facility at the Rutherford-Appleton Laboratories (UK). Here we report a brief explanation of the setup and its technical specifications. More deatils can be found in [et al., 2009].

The availability of tunable, femtosecond pulses at wavelengths spanning the ultraviolet to the infrared had a great impact in the physics of the materials. In the past, most studies of strong field interactions on an ultrafast timescale have been at 800 nm, restricted by the gain spectrum of Ti:Sapphire based systems. As laser technology moves to higher repetition rates, the feasibility of using XUV pulses in the 10-100 eV energy range created through high harmonic generation increases. The shot-to-shot stability of the harmonics improves and the average photon flux increases to the point where complex experiments, such as photoemission measurements, requiring averaging over many thousands of laser shots become possible. The Artemis facility for ultrafast XUV science at the Central Laser Facility in the UK aims to capitalise on these advances by bringing them together in combination. The facility provides few-cycle, carrier-envelope phase stabilised and tuneable laser beamlines, XUV beamlines and interaction stations for gas-phase and condensed matter experiments. A scheme of the entire setup is shown in Figure 5.9.

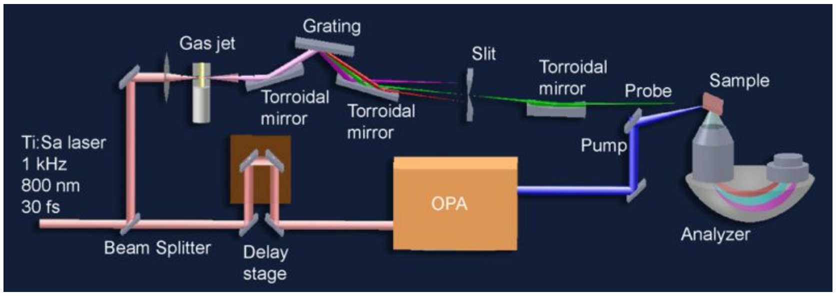

Figure 5.9: Simplified sketch of the XUV time-resolved photoemission setup. MIR pump is achieved by an optical parametric amplifier setup. XUV probe is obtained via HHG generation in argon gas, ranging from 10 to 40 eV. The probe beam is selected by a grating setup, and focused by a toroidal mirror. Electrons are detected by a hemispherical analyzer, which enables the detection of energy and momentum simultaneously.

Artemis is constructed around a carrier-envelope phase (CEP) stabilised femtosecond laser system. This can be used to generate tunable pulses across a wavelength range spanning the UV to the far infrared, few-cycle pulses at 800 nm and short pulses of XUV radiation through high harmonic generation (HHG). The XUV can be delivered to interaction stations for materials science and atomic and molecular physics through vacuum beamlines for broadband or monochromatic (narrowband) XUV pulses. The Artemis facility provides a variety of ultrafast, synchronised laser beamlines which can be configured flexibly either to generate XUV or as pump and probe pulses spanning the UV to far infrared. The core of the facility is a 14 mJ, 30 fs, 1 kHz Ti:Sapphire CPA system operating at 785 nm. Tuneable pulses spanning the spectral range from 230 nm to 20 microns are provided by an optical parametric amplifier (HE-Topas from Light Conversion). This is pumped with up to 8 mJ of the output from the laser system. At 1300 nm, it can achieve pulse energies of up to 1 mJ (1 W average power at 1 kHz) and a pulse duration of 40 fs. This enables focused intensities exceeding 10^{14} Wcm-2 to be achieved.

XUV radiation in the wavelength range 10-100 nm (10-100 eV) is produced through high harmonic generation (HHG) in a gas target. The resulting XUV radiation has similar pulse-duration to the drive laser pulse and is synchronised to the drive laser pulse with sub-fs resolution. With conversion efficiencies up to 10^{-6} at 30 eV, a photon flux of up to 10^{11} photons s^{-1} per harmonic is achievable. For experiments requiring wavelength and bandwidth selection, Artemis provides a narrow-bandwidth, tunable XUV beamline. In this beamline the harmonics pass through a state of the art XUV monochromator, which enables a single harmonic, or narrower bandwidth, to be selected from the spectrum, while maintaining the femtosecond pulse-duration. Figure 5.10 shows the scanned HHG spectrum obtained with a grating of the XUV monochromator.

The Artemis Materials Science end-station is designed for time- and angle-resolved photoemission spectroscopy. The end-station is a UHV chamber, which pumps to <2x10^{-10} mbar, equipped with a hemispherical electron analyser (SPECS Phoibos 100) and two-dimensional detector for energy- and angle-resolved measurements with an energy resolution of ∼5 meV and an angular resolution of <1 degree. A liquid-helium-cooled, five-axis manipulator enables the sample to be cooled to 14 K or resistively heated to 1000 K.

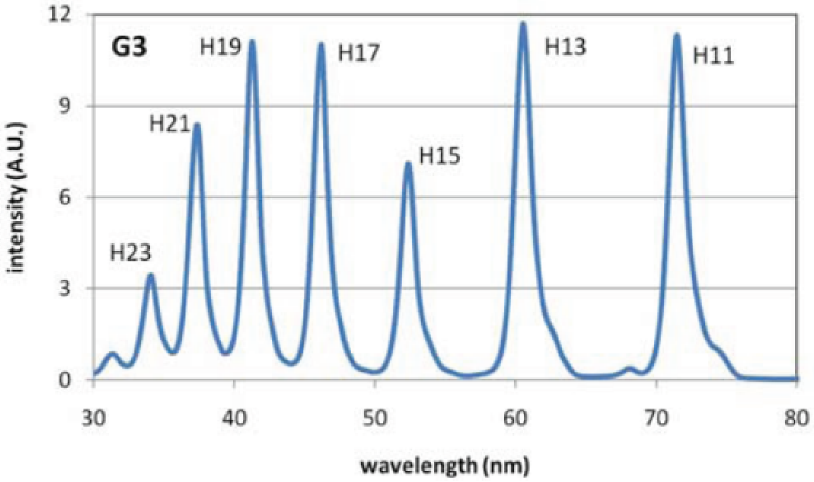

Figure 5.10: HHG spectrum generated with 1 mJ of 800nm radiation in argon, obtained using the monochromator. [et al., 2009]